Highlights

Decomposition and Inference of Sources through Spatiotemporal Analysis of Network Signals: The DISSTANS Python Package

Tobias Köhne,Bryan Riel,Mark Simons

- DISSTANS is a Python package optimized for the decomposition of GNSS timeseries
- DISSTANS includes a variety of decomposition approaches
- DISSTANS can incorporate spatial correlation a priori in the analysis
- DISSTANS offers visualization tools, is easily extendable, and can be automated
- DISSTANS is generic, fast, open-source, and well-documented

Decomposition and Inference of Sources through Spatiotemporal Analysis of Network Signals: The DISSTANS Python Package

Tobias Köhne[a,*], Bryan Riel[b] and Mark Simons[a]

[a]*Seismological Laboratory, Division of Geological and Planetary Sciences, California Institute of Technology, 1200 E California Blvd, Pasadena, 91106, CA, USA*

[b]*Department of Earth, Atmospheric and Planetary Sciences, Massachusetts Institute of Technology, 77 Massachusetts Avenue, Cambridge, 02139, MA, USA*

ARTICLE INFO

Keywords:
Geodesy
GNSS
Python

ABSTRACT

Dense, regional-scale, continuously-operating Global Navigation Satellite System (GNSS) networks enable the monitoring of plate motion and regional surface deformation. The spatial extent and density of these networks, as well as the length of observation records, have steadily increased in the past three decades. Software to efficiently analyze the ever-increasing amount of available timeseries should be geographically portable and computationally efficient, allow for automation, use spatial correlation (exploiting the fact that nearby stations experience common signals), and have openly accessible source code as well as documentation. We introduce the DISSTANS Python package, which aims to be generic (therefore portable), parallelizable (fast), and able to exploit the spatial structure of the observation records in a user-assisted, semi-automated framework that includes uncertainty propagation. DISSTANS is open-source, includes an application interface documentation as well as usage tutorials, and is easily extendable. We present two case studies that demonstrate our code, one using a synthetic dataset and one using real GNSS network timeseries.

1. Introduction

Networks of Global Navigation Satellite System (GNSS) stations enable the direct observation of surface displacement down to millimeter accuracy (e.g., Blewitt, 2015). Originally using only the Global Positioning System (GPS) and consisting of only a handful of stations, modern quasi-permanent deployments sometimes incorporate more than 1,000 receivers and take advantage of other GNSS constellations such as the European Galileo or Chinese BeiDou systems. Analyzing network position timeseries requires awareness of the many processes that affect the observations, both desired and confounding, and an ability to distinguish between them. While dominant constituents like the secular motion of a particular station can usually be inferred by simple linear regression, quantifying less prominent constituents (e.g., displacements due to low-magnitude slow fault slip events or small-volume magma chamber pressurization) requires a better understanding of the contributing processes.

Here, we present the Decomposition and Inference of Sources through Spatiotemporal Analysis of Network Signals (DISSTANS) Python package to facilitate the temporal and spatial decomposition of GNSS timeseries. The code is written in a generic, fully object-oriented fashion with minimal assumptions as to study location, data units, and sampling frequency. Different data loading methods are implemented that interface with common existing timeseries file formats, but are also easily adapted to new formats. All downstream processing is independent of the original format and origin. To make the code as usable and accessible as possible, it is open-source and extensively commented. The repository includes tagged versions, verbose commit messages, and full documentation. The documentation features tutorials based on synthetic and real timeseries data, a subset of which are presented here. DISSTANS already contains many common processing workflows. These workflows are usable with just a few lines of code, and more are in the planned development roadmap. DISSTANS is parallelized for the most demanding tasks — most notably the model fitting component. We also provide extensive plotting options and graphical user interfaces, simplifying interactions with the data.

Section 2 of this report introduces some key structural decisions and presents a brief literature review of previous work, placing this study in the broader scientific context. Section 3 provides an overview of the code design, with Appendix A detailing the lower-level implementation. To validate our processing, Section 4 contains the analysis of a synthetic network of GNSS stations, as well as results from a real-world application using data from the Long Valley Caldera region, California, USA. Section 5 discusses key design choices. Finally, we end in Section 6 with a brief summary and some possible future avenues for extensions to DISSTANS.

2. Background

The list of scientific questions that can be addressed with GNSS networks is long, and the list of approaches that can be used is even longer (e.g., Blewitt et al., 2018; Herring et al., 2018; Bertiger et al., 2020; Herring et al., 2016). For studies of plate motion, surface deformation, and related fields, the key data are displacement timeseries, i.e.,

---

✉ `tkoehne@caltech.edu` (T. Köhne); `briel@mit.edu` (B. Riel); `simons@caltech.edu` (M. Simons)

ORCID(s): `0000-0002-8400-7255` (T. Köhne); `0000-0003-1940-3910` (B. Riel); `0000-0003-1412-6395` (M. Simons)

the relative movement over time of a receiver with respect to a defined reference frame. To obtain these timeseries, processing centers start from raw receiver observables (time, pseudoranges, and phases) and take into account a large number of physical processes (e.g., tropospheric and ionospheric travel time delays, gravitational effects, relativistic effects) to produce the best estimate of true receiver position for any given sampling interval (e.g., daily or hourly); see, for example, Misra and Enge (2010) or Blewitt (2015).

With these displacement timeseries, we can now interrogate the timeseries: Is the entire signal explained by rigid plate motion (e.g., Altamimi et al., 2017)? What are the causes for shortterm or longterm transients (e.g., Houston et al., 2011)? How can we use inter-, co- and postseismic station velocities to constrain fault locking (e.g., Meade and Hager, 2005)? Similarly, one might also want to identify and characterize noise processes (e.g., power-law noise, Langbein, 2020). All of these questions, however, require the *decomposition* of the timeseries into components that are the direct effect of specific physical processes (e.g., hydrological seasonal loading, earthquake offsets and transients, plate motion), and a residual component which is the result of noise processes, processing artifacts, and imperfect modeling.

In this study, we focus on this intermediate step, and refer to it as simply *timeseries decomposition*. Therefore, we will refer to the displacement timeseries as produced by GNSS network processing centers as the *raw* or *input* timeseries, and the decomposition process will aim to isolate timeseries *constituents*.

2.1. Approaches to Timeseries Decomposition

We categorize timeseries decomposition tools using three main criteria.

2.1.1. Process-aware vs. process-agnostic

This first criterion aims to distinguish approaches that either make a priori assumptions about the physical processes affecting the data (expecting a certain structure in the data), or alternatively, assume the least possible. For example, fitting a model containing a complete set of basis functions to a timeseries is, in its most generic form, process-agnostic (e.g., Riel et al., 2014), but fitting a logarithmic decay function to a postseismic transient effectively assumes a specific tectonic process (e.g., Hsu et al., 2009).

Process-agnostic approaches will usually achieve the "best" fit to the observations — at least as measured by the magnitude of the residuals, since that is the principle optimization criterion for such methods. However, overreliance on the data and its residuals makes these methods susceptible to "overfitting"; i.e., interpreting noise as signal. Process-agnostic methods also have difficulties determining trade-offs between different source processes, for example in the case of Principal Component Analysis (PCA) when signals manifest in multiple principal components, or a single principal component mixes different signals. In contrast, process-aware approaches might ignore parts of the observation if they either (a) do not have an appropriate way of describing the observation (e.g., an unexpected transient), or (b) try to fit a signal with an inappropriate model (e.g., mapping postseismic deformation into the coseismic one); as these approaches naturally prefer a decomposition that follows the assumed underlying functional forms.

2.1.2. Parametric vs. non-parametric

This second criterion assesses whether one estimates parameters (coefficients) for predetermined models to decompose the timeseries. The models can be as complex as desired (high dimensionality, non-linear). Examples for non-parametric decompositions are linear time-invariant filters used in signal processing (e.g., bandpass or lowpass filters) or basis reprojections like Principal Component Analysis (PCA), Independent Component Analysis (ICA), or Singular Spectrum Analysis (SSA).

Note that this criterion ignores the impact of hyperparameters (e.g., regularization penalties, frequency windows). With non-parametric approaches, the assumptions and hyperparameters are minimal compared to model-based methods, thereby simplifying the problem setup immensely. Furthermore, reducing the influence of hyperparameters translates into a reduction of possible sources of errors. On the other hand, parametric approaches enable a straightforward implementation of the formal covariances between model parameters, and by extension, uncertainties in the predicted timeseries. These approaches can also deal naturally with data gaps (i.e., without the need for data imputation). Crucially, a parametric approach is necessary for process-aware studies, because non-parametric approaches have no inherent knowledge about how to group different source processes into components (see above).

2.1.3. Station- vs. network-level

An additional criterion acknowledges the role that spatial information can play in the analysis process. For example, if the same models are fit to every timeseries in a network, regardless of where the stations are located, then the decomposition code is not aware of the spatial context. These local, station-level solutions are therefore independent from another. If one recognizes, however, that geophysical signals usually have a spatially coherent signature (assuming sufficiently dense networks), then we can and should incorporate that understanding. For example, PCA makes use of the fact that all stations in the network can potentially see the same source signal (even though the network geometry is neglected). Taking advantage of potential spatial structure can be beneficial, although the complexity of the resulting code and additional computational costs are not negligible.

2.2. Review of Existing Tools

Considering the diversity of possible approaches, the selection of a certain approach (or the design of a hybrid approach) depends on one's goals and the available data. Additional factors include the ease of software implementation, or possibilities to extend the methods to include ancillary datasets (e.g., rainfall, earthquake catalogs, atmospheric pressure). We review selected published work in the field of timeseries decomposition in the context of process-agnostic vs. process-aware, parametric vs. non-parametric, and degree of spatial awareness.

Before high-quality station timeseries became ubiquitous, the QOCA software (Dong et al., 1998) could be used to combine "quasi-observations" (lightly-processed input data from GPS, Electronic Distance Measurements, Satellite Laser Ranging, or Very Long Baseline Interferometry) using a Kalman filter approach. QOCA includes the module `analyze_tseri` to estimate linear, episodic, and stochastic motion of the different stations individually in a least-squares-based, process-aware, and parametric framework.

With an increasing number of GNSS stations, more GNSS constellations, and more precise understanding of the physical processes affecting GNSS positioning solutions, GNSS networks became common for monitoring surface deformation. Today, the analysis tools developed to produce GNSS displacement timeseries routinely also include simple timeseries decomposition functionality. For example, the current iterations of JPL's GipsyX/RTGx (Bertiger et al., 2020) and MIT's GAMIT/GLOBK (Herring et al., 2018) software both contain methods to estimate position, velocity, seasonal variations, offsets[1], and postseismic deformations[2]. These Kalman-filter-based methods are parametric, process-aware, but in contrast to QOCA, not spatially aware.

For regions where complex geophysical processes are at play (such as near a volcano or in subduction zones), more complex analysis is necessary to distinguish between different processes. A common example is the impact of an un unmodeled transient period on the estimated secular plate velocity. In the following, we present a (non-exhaustive, unordered) small selection of tools that start from raw GNSS displacement timeseries to analyze stations exhibiting more complex behavior.

The Network Inversion Filter (NIF), first proposed by Segall and Matthews (1997) and subsequently expanded upon by a variety of studies (e.g., McGuire and Segall, 2003; Bekaert et al., 2016), estimates slip rates on predetermined fault structures from (GNSS or other) observations using a Kalman filter. It is therefore process-aware, and because slip on the modeled faults affect multiple stations, which are jointly used to estimate the slip coefficients, it is also spatially aware. The NIF estimates slip and therefore transient displacement constituents non-parametrically, but the hyperparameters specifying the fault geometry and the characteristics of fault slip in time and space (e.g., smoothness) play an important role.

The Median Interannual Difference Adjusted for Skewness (MIDAS, Blewitt et al., 2016) algorithm explicitly recognizes the importance of unmodeled steps and shortterm transient deformation in the raw timeseries. Not being a traditional regression scheme, it uses the median of velocities computed from data pairs separated by one year, providing a degree of insensitivity to offsets, small data gaps, and annual seasonal signals if the timeseries is sufficiently long. This process-aware, station-level method is mostly defined by its hyperparameters, although other parameters such as known maintenance and earthquake offset times are used. It is therefore a powerful, largely automated method to estimate secular plate velocities, that does not attempt to extract non-annual seasonal, transient, or decaying signals. MIDAS is at the core of UNR's Nevada Geodetic Laboratory openly-accessible global GNSS timeseries repository (Blewitt et al., 2018).

The Señales y Análisis de Ruido Interactivo (Interactive Signal and Noise Analysis, SARI, Santamaría-Gómez, 2019) software performs process-aware, parametric, station-level regression focusing on an interactive user interface. least-squares or Kalman filtering is used to fit polynomial, sinusoidal, exponential, logarithmic, and step models, allowing for a detailed timeseries decomposition. It also contains useful additional functionality such as automatic discontinuity detection, periodogram visualization, and noise characterization.

The Greedy Automatic Signal Decomposition (GrAtSiD, Bedford and Bevis, 2018) algorithm is an iterative, station-level method that focuses on detecting and modeling transient signals in the timeseries. At each iteration, a least-squares regression is performed that includes a linear trend, sinusoidal oscillations, predefined steps, as well as a selection of sparse, transient functions ("multitransients"). Only multitransients that significantly improve the data fit are kept for the next iteration, until a convergence criteria is reached. GrAtSiD can therefore be classified as a parametric approach, that is partly process-aware (for the non-multitransient parts of the regression) and partly process-agnostic (since the multitransients can have a variety of shapes and are not tied to a particular physical source).

MIDAS, SARI, and GrAtSiD are limited to station-level model fit solutions, and do not incorporate spatial awareness.

An example of a non-parametric, process-agnostic, and spatially-aware method to decompose timeseries is the variational Bayesian Independent Component Analysis (vbICA, Gualandi et al., 2016), a modern iteration of basis reprojection algorithms particularly suitable for GNSS networks. Its key distinction from traditional PCA/ICA is to recognize that probability density functions for individual components are generally not normally distributed by nature, and alleviates this problem by using mixtures of Gaussians. vbICA therefore allows for a more accurate signal separation, as well as a formal way to incorporate component uncertainties.

Riel et al. (2014) proposed a method that builds on parametric, process-aware regularized regression. Their approach adds a process-agnostic set of B-Spline functions to model transients in a spatially-aware framework. DISSTANS builds on this framework, which we describe in more detail in Sections 3.2 and 3.3.

Here, we have just described a subset of available tools, focusing on publicly available, complete software packages that provide a reasonable level of portability. There are many other studies that have implemented or adapted codes and methods for specific study regions or purposes; an analysis

---

[1] Automatic detection only by GipsyX.

[2] Only GAMIT/GLOBK.

and comparison of which would be beyond the scope of this work.

3. Code Overview

DISSTANS aims to build on advancements and best practices of previous work, combining them into a single package that adheres to standards of free, extensible, shareable, and scalable software. At its core, it models timeseries as the linear combination of constituent functions, and estimates the functions' coefficients using least-squares. DISSTANS also includes a suite of pre- and postprocessing tools. In this section, we present key properties and design choices made in the DISSTANS package (Section 3.1), as well as two core functionalities (spline-based transient modeling and spatial regularization, see Sections 3.2–3.3). More implementation details can be found in Appendix A.

3.1. Goals

Commonly-used workflows included. To allow researchers to focus more on science and less on programming, timeseries decomposition software should include easy-to-use versions of well-established timeseries decomposition workflows. Such software can then be used for generic pre- and postprocessing, as well as serve as a base on which new analysis methods can be developed. An additional benefit of comprehensive software is the lowering of the entry barrier for researchers new to the field. DISSTANS therefore provides a vast array of such workflows, ranging from data cleaning methods and PCA/ICA decomposition to simple least-squares fitting with standard models and residual analysis.

Incorporating process knowledge. Where knowledge about physical processes affecting GNSS timeseries is present (e.g., an inflating magma chamber), such information can theoretically improve model fitting. It is therefore desirable for timeseries decomposition methods to both include models that best represent known physical processes, as well as methods that are flexible enough to account for unmodeled, unknown processes. DISSTANS allows for such a distinction by offering a range of process-aware, as well as process-agnostic models (see Section 3.2 and Appendix A.2).

Spatial awareness. With GNSS networks becoming more widespread — and more importantly, denser — we should explicitly recognize that nearby stations subject to common geophysical processes may behave similarly. If we only consider each station individually, we may miss the opportunity to identify constituents that manifest themselves around the noise floor. However, if many stations experience the same signal (with different magnitudes), a joint estimation can theoretically enhance our ability to detect them. Such a method would thereby lower the effective signal-to-noise ratio necessary for constituent extraction. DISSTANS allows one to take advantage of the available spatial information by building on the spatiotemporal transient fitting algorithm developed by Riel et al. (2014) (also see Section 3.3 and Appendix A.3).

Scalability. In order to scale well with both the number of stations, as well as the length of the observation record, it is useful to parallelize the computationally demanding parts. DISSTANS includes an option to parallelize the station-level, least-squares solutions, as well as the evaluation of the predicted model timeseries including the full model covariance matrix.

Uncertainty estimation. Given the possible complexities of displacement timeseries, a proper interpretation of signal decomposition results can only be made if the trade-offs between and within models and east-north-up components can be quantified. The full, formal model covariances can be estimated and propagated in the DISSTANS workflow.

Step detection. One omnipresent challenge when analyzing timeseries is the detection and subsequent estimation (or equivalently, removal) of steps in the data. Improper step removal can significantly affect secular plate velocities as well as the character of GNSS noise (e.g., Santamaría-Gómez and Ray, 2021; Blewitt et al., 2016), but there is no fully-automated algorithm that would remove the need for manual inspection (e.g., Gazeaux et al., 2013). DISSTANS contains semi-automated tools that aid modeling all relevant offsets: a step detector (similar to the one in GipsyX, Bertiger et al., 2020, also see Appendix A.6), a visualization GUI to inspect the data (see Appendix A.8), and loading functions for maintenance records in multiple formats. DISSTANS also features both an empirical (following Blewitt et al., 2016) and an elastic-half-space-based method to determine whether or not to allow a coseismic offsets to be estimated at any given station and time.

Portability and extendability. As new GNSS networks are built, and output formats of data processing centers change, one must be able to easily incorporate these changes. DISSTANS separates the data loading tasks from all other analysis steps, such that the former can easily be updated without affecting the latter. Furthermore, to enable the development and integration of new approaches, DISSTANS is written as a modular, extendable framework (in contrast to single-use collections of scripts, see Appendices A.1 and A.4).

3.2. Spline-Based Transient Modeling

To optionally model transient signals in the displacement timeseries of unknown functional shape, DISSTANS includes spline-based models. *B-splines* in particular are piecewise-polynomial functions that, when constructed in a specific manner, form a full basis for any polynomial function of a given degree over the basis' support. As introduced by Hetland et al. (2012) for geophysical applications, sets of repeated, uniform, integrated B-splines (see Fig. A2 for a visualization) of various timescales and center times can be used to approximate any given unknown transient signal of similar timescales. The ability to approximate arbitrary functions in a process-agnostic framework makes sets of splines useful for timeseries decomposition where standard functions (polynomials, sinusoids, exponential functions, etc.) cannot capture the full breadth of the observations (e.g., aseismic slow slip or volcanic expansion events). A more detailed mathematical description of the available spline-based models in DISSTANS can be found in Appendix A.2.

3.3. Local and Spatial Regularization

Sets (or "dictionaries") created by shifting and scaling a single uniform B-spline are not linearly independent (see Hetland et al., 2012), and therefore do not form a "proper" basis in the mathematical sense. It follows that any signal decomposition using such sets is non-unique, and thus requires regularizing the solution. The most commonly used regularization is based on the L2 (Euclidean) vector norm $\|\cdot\|_2^2$, promoting solutions with smaller overall magnitudes. However, in the context of fitting transient signals that may or may not be present in the timeseries, we prefer a regularization scheme that yields sparse solutions, i.e., spline coefficients should be driven to zero if there is not sufficient evidence in the data to warrant usage of any given spline in the overall model fit. L1-norm regularization is such a sparsity-promoting regularization scheme: it penalizes the absolute magnitudes $\|\cdot\|_1$ of the estimated parameters, driving many parameters close to zero. L0-norm regularization goes further by penalizing the *existence* $\|\cdot\|_0$ of a parameter, thereby either driving parameters to zero, or not penalizing a parameter at all (Candès et al., 2008). This type of regularization is therefore more suited for physical processes which occur sporadically, are not ubiquitous, and have an "arbitrary", but significant, magnitude. All three regularization schemes are implemented in DISSTANS (see Appendix A.3).

Riel et al. (2014) combined the potential of using dictionary of splines with the benefits of L0 regularization. Using the algorithm introduced by Candès et al. (2008), they proposed a method to extend the regularization from a timeseries at a single station (henceforth referred to as *local* L0 regularization) to all the timeseries in a network of stations (*spatial* L0 regularization). Their approach yields spline-based fits whose estimated model coefficients are sparse in time (i.e., for a single timeseries at one station) *and* space: transient signals common to multiple stations are decomposed using the same spline functions. An additional benefit of a spatially-coherent set of splines is that it is harder for the solver to fit local noise processes with splines that would only be relevant at isolated stations and times. DISSTANS builds on the method of Riel et al. (2014) (for which the relevant source code was never published), extending it in various ways (most notably, adding parallelization and improving the numerical stability). More details on the implementation of the spatial L0 regularization can be found in Appendix A.3.

4. Validation

We present two validation datasets and results. The first, in Section 4.1, is a synthetic dataset of 16 stations exhibiting some commonly seen patterns in GNSS network timeseries. Using this synthetic network, we demonstrate key capabilities of this code in estimating spatially-coherent complex signals, all while being able to compare fitted models to the true underlying timeseries. The second dataset, in Section 4.2, is a collection of GNSS stations in the Long Valley Caldera region in California, USA. Here, the main goal is to recover the transient caldera inflation signal, and discuss some subtleties in the analysis when dealing with imperfect, real-world data.

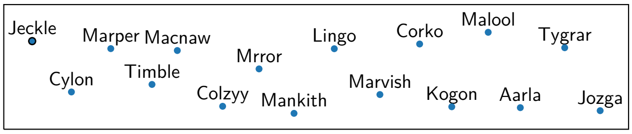

Figure 1: Map view of the synthetic network.

4.1. Synthetic Dataset

The code for this analysis, as well as additional discussion, can be found in Tutorial 3 of the online documentation.

A key feature of DISSTANS is its ability to use spatial coherence as an additional source of information and constraint. In general, signals like earthquakes, slow fault slip events, or seasonal loading are spatially correlated, as the processes affecting each station have the same underlying sources. By using this knowledge in combination with the enforcement of sparsity, we ensure that the estimated models are consistent between stations. Processes that only affect a single station are considered noise for the purposes of this study (e.g., antenna maintenance or strongly localized displacements).

4.1.1. Setup

The synthetic dataset is comprised of 16 stations randomly positioned on an elongated, rectangular grid (see Fig. 1). Each two-component station is affected by a secular, linear trend, one annual seasonal signal, an earthquake (with both co- and postseismic components), two shortterm slow slip events, one longterm transient, common mode error, and measurement error (correlated between the components). The linear trend, coseismic and postseismic constituents are all equal in direction and magnitude, whereas the seasonal constituent is random at each station. The three transients are all equal in onset time, duration, and direction, but differ in magnitude. Furthermore, one station ("Cylon") experiences significant powerlaw noise, and a different station is affected by an unmodeled maintenance step. Both signals represent site-specific noise processes that the spatial coherence constraint aims to suppress. Lastly, the amplitudes of the three transients decrease exponentially towards the east.

The analysis follows a simplified version of the example workflow presented in Appendix A.7. Because the data is synthetic, no quality metrics need to be applied, nor is step detection necessary. We add the following constituents to our inversion: polynomial, sinusoidal, step, and logarithmic (to recover everything except the transients; unregularized); and a set of splines. To recover the transient episodes, the spatially-regularized splines contain timescales between a

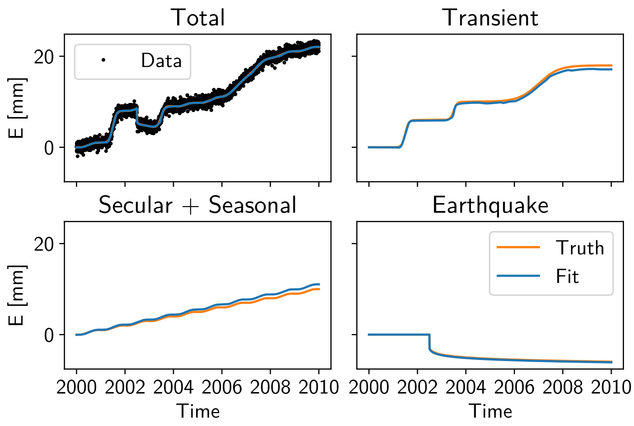

Figure 2: Overall model fit to the data at station Jeckle (see Fig. 1), including the decomposition into the primary constituents (East component only).

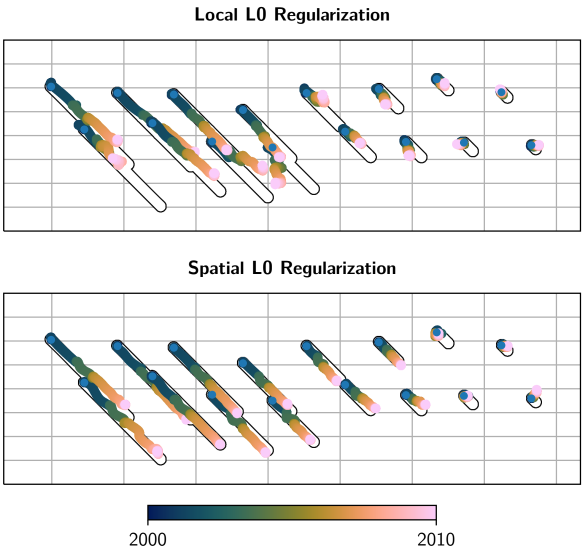

Figure 3: Map view of the transient motion of the synthetic network over the entire timespan. The top panel shows the result without spatial regularization, the bottom one with. Markers correspond to the position of a station relative to its initial position, with colors corresponding to time. The white background curves with black outlines are the true synthetic transient, which is clearly better matched by the solution incorporating spatial awareness.

month and multiple years, amounting to hundreds of individual splines (see Fig. S4). The fitting converges smoothly onto the final solution (see Fig. S1). In the following, we compare the results obtained using local and spatial L0 regularization to highlight the benefits of promoting spatial coherence.

4.1.2. Results

Fig. 2 shows the East component of a representative station. The inferred model fits the synthetic data well. We find a small tradeoff between the secular and transient constituents, although we note that in real world applications, such a conclusion is frequently difficult. (A visualization of the full model parameter correlation matrix can be found in Fig. S2.) Fig. S5 and Table S1 present comparison results of our spatial L0 solution with the L0 solution without spatial regularization (see below) and other commonly used methods (simple least-squares, MIDAS), showing that the spatially-aware L0 solution clearly outperforms other methods.

Fig. 3 shows the improvement from local to spatial L0 regularization in map view for all stations: the transient components are smoother (therefore fitting less noise) and more closely follow the true signal (shown in the background). Importantly, the homogenous displacement field is obtained without degrading the fit to the data (compare Fig. S3). This is enabled by the spatial solver's identification of the set of splines that best describes the transient signal common to all stations (compare Fig. S4), and the better recovery of the secular velocity. Section S.2 explores the dependence of the model error on the number of stations for a different synthetic network, with Fig. S6 further validating our claim that incorporating information from nearby stations improves the quality of the resulting model fit.

4.2. Long Valley Caldera

The code for this analysis, as well as additional discussion, can be found in Example 1 of the online documentation.

To demonstrate DISSTANS with real data, we consider timeseries from the Long Valley Caldera (LVC) region in California, USA. Because of the geophysical interest into the magmatic, seismic, and hydrological processes at work there, the LVC has been monitored by an ever-expanding network of GNSS stations since the late 1990s (e.g., Ji et al., 2013; Montgomery-Brown et al., 2015; Silverii et al., 2020). The displacement timeseries are complemented by detailed maintenance and seismic catalogues, which are crucial for determining the best set of steps to include in the fitting process. In this example, the goals are threefold: (1) to illustrate the example workflow proposed in Section A.7, (2) to present the best-fit transient model to the periods of unrest in the Long Valley Caldera, and (3) to showcase the importance of allowing the seasonal signal models to vary in amplitude over time. Any in-depth physical modeling of the extracted constituents is beyond the scope of this study.

4.2.1. Setup

The data and corresponding maintenance and seismic events catalog are downloaded with DISSTANS-included tools from the GNSS timeseries repository maintained by the University of Nevada at Reno's Nevada Geodetic Laboratory (Blewitt et al., 2018). Only stations with a reliability of over 50% (i.e., observations on more than half of the days the station was active) and an observation record at least one year long are considered, and outliers in each timeseries (more than 10 standard deviations away from the median) as well as the common mode error are removed. With help of the available maintenance catalog, we iteratively identify steps in the data. This process is aided by the step detector

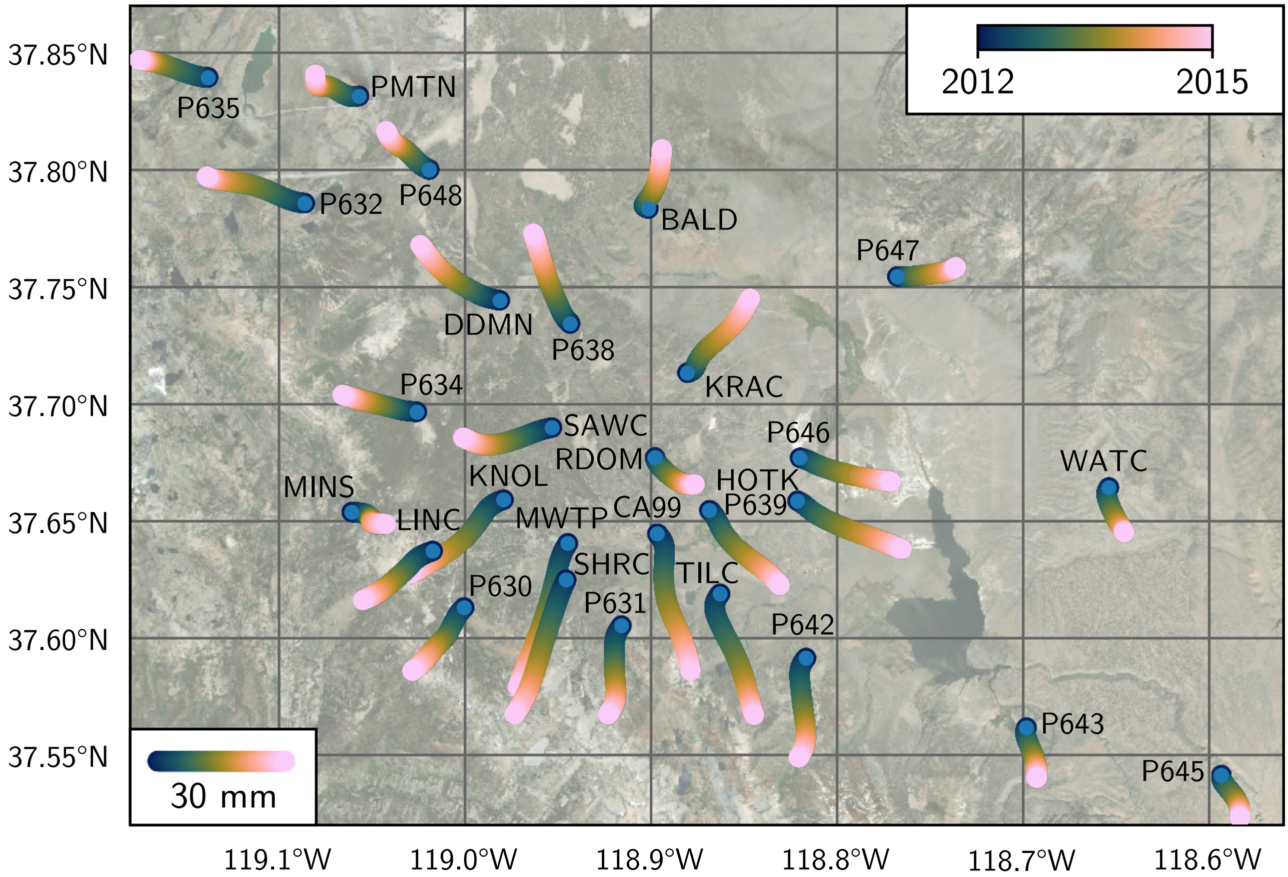

Figure 4: Modeled horizontal transient displacements of selected stations in the Long Valley Caldera region during the period between 2012 and 2015. The traces begin at the nominal location of each station, with the color of the markers corresponding to the time. Background satellite imagery by Earthstar Geographics & Esri.

and visualization routines included in DISSTANS. For the final fit, we use following models: polynomial, sinusoidal, and steps (to recover everything except the transients; unregularized); a set of splines (to recover the transient episodes, containing timescales between months and multiple years, hundreds of individual splines; spatially regularized); and a varying-amplitude sinusoid (for deviations from the nominal, unregularized seasonal signal; locally regularized).

4.2.2. Transient Signals

The timespan between 2012 and 2015 (approximately) is dominated by a significant expansion of the caldera's dome, as observed by both the GNSS network and Interferometric Synthetic Aperture Radar (InSAR) timeseries (Montgomery-Brown et al., 2015; Silverii et al., 2020). Fig. 4 shows the horizontal component estimated by DISSTANS in map view: the radial extension of the network from the center of the dome is clearly visible.

Fig. 5 shows the extracted transient constituent of selected stations in and around the resurgent dome for the entirety of the available data. Two periods of significant expansion can clearly be distinguished: around 2002–2003, and from 2011–2021. A smaller period of unrest can be seen throughout the network between approximately 2008–2010, and the station CASA allows us to see a period of extremely rapid expansion around 1998. These results are comparable to Silverii et al. (2020, Fig. S3a), where transients were recovered using non-parametric multiyear filters, even though the directions of maximum displacements are different. Crucially, however, we did not enforce the secular long-term motion to be zero during a specific timespan. As a result, many stations appear to never reach a "steady-state" matching the general plate motion, because the transient motion, even when regularized, is dominant for large parts of each timeseries. (A priori removal of a secular trend can easily be done with DISSTANS, if desired.)

Estimation of the transient signal directly affects the secular velocity estimate, for which different published values for the stations in and around the Long Valley Caldera exist, which in turn enables a more straightforward validation than comparing extracted transients between methods or studies. In Section S.3, Figs. S7–S9, we compare our results with the MIDAS-derived secular velocities (Blewitt et al., 2016) and the Geodesy Advancing Geosciences and EarthScope (GAGE) facility's secular velocities (Herring et al., 2016).

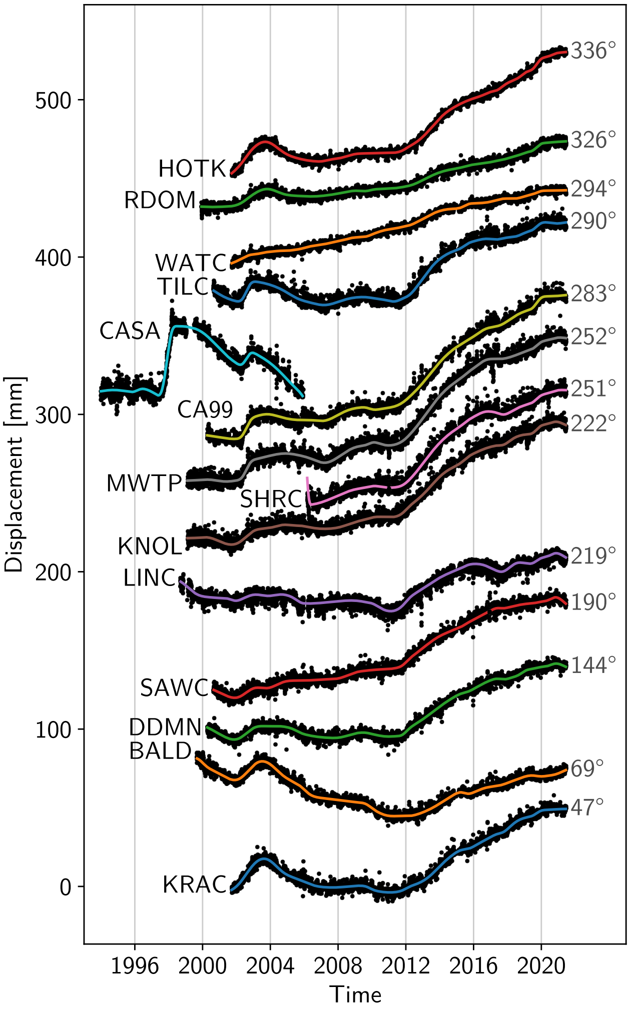

Figure 5: Modeled horizontal transient displacement (colored lines) of selected stations (names on the left) from Fig. 4, projected along the direction of maximum displacement during the period of 2012–2015. The directions (in grey to the right of the timeseries) are measured counterclockwise from east. CA99's direction is used for CASA. Black dots are the joint model's residuals, centered on the transient model.

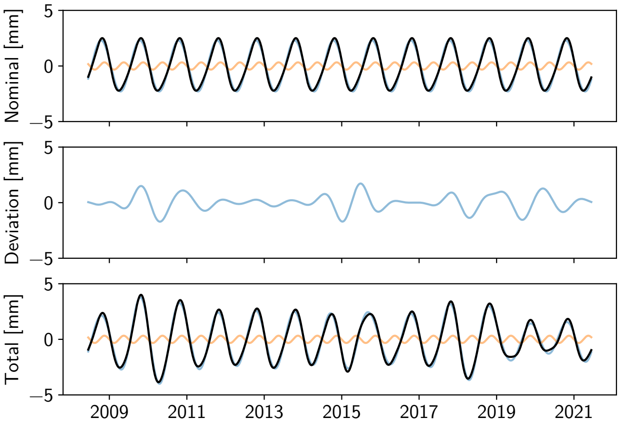

Figure 6: Modeled seasonal vertical displacement timeseries for station P647 (see Fig. 4 for location). Blue and orange lines correspond to the annual and biannual constituents, respectively, and the black line is their sum. The deviation component only includes the annual frequency.

4.2.3. Seasonal Signals

Traditional least-squares model fitting for GNSS timeseries usually either approximate the seasonal signal as having a constant amplitude and phase over the entire timespan considered (or piecewise within that timeseries) (e.g., Heflin et al., 2020), or estimate a more accurate seasonal deformation signal from filtering or component-analysis methods (e.g., Silverii et al., 2020). The two approaches are usually acceptable, as either the resulting residuals are insignificant, or are not prone to producing large seasonal residuals in the first place. Given our transient modeling of even small timescales (down to the order of less than 100 days), our method does suffer from these seasonal residuals, as annual rain- and snowfall can vary widely, especially in the Sierra Nevada. In fact, because seasonal residual are highly correlated between stations, they are not removed by our spatial L0 regularization. Modeling the seasonal signal as the sum of both an unregularized, constant, nominal constituent, and a simple, L1-regularized, station-specific deviation constituent of the same nominal frequencies that is allowed to vary in amplitude (and by construction, instantaneous phase) over time, the solver is once again able to separate seasonal (i.e., periodic) signals from (aperiodic) transient motion (see Appendix A.2). One example of the resulting seasonal fit in the vertical direction is shown in Fig. 6. Variations in the amplitude, and sometimes instantaneous phase, are clearly visible, demonstrating the importance of properly estimating and removing the seasonal signal at stations that are affected by major hydrological processes. Fig. S10 shows the annual model's vertical amplitude and phase in map view, and Fig. S11 shows the overall vertical seasonal constituent for the stations in Fig. 5 for the entire timespan.

5. Discussion

The choice to incorporate process-agnostic, spatial awareness into the timeseries decomposition problem by means of a parametric, spline-based model that requires regularization and iteration may possibly appear odd — after all, vbICA and comparable methods already have an inherent sense of space. However, even though basis decompositions have a spatial component, the geometry of the network is neglected (e.g., relative distance between stations). Network geometry and extent become relevant when networks are large, and some signals are spatially confined: different processes at different locations may be mapped into the same component, complicating its interpretation. Furthermore, in order to obtain a clean decomposition using vbICA or similar methods, maintenance and earthquake coseismic offsets still have to be removed ahead of time, as well as the linear secular trends. Therefore, not only do these non-parametric decomposition approaches require a significant amount of preprocessing in the first place, the separation of preprocessing and actual decomposition precludes a straightforward way to quantify the covariance between the constituents. Using parametric models that are both process-aware (such as secular, seasonal, and maintenance offset models) and process-agnostic (using a dictionary of splines for transients and seasonal variations), by contrast, offers this correlation by design, while the spatial L0 regularization accomplishes the goals for sparsity and spatial awareness. We note that DISSTANS still does offer PCA/ICA, for example used for the common mode removal.

Parametric approaches allow one to include prior knowledge beyond the preprocessing steps. Incorporating such knowledge is already partly possible through the choice of the model functions (e.g., inserting a postseismic displacement model after a large earthquake), but least-squares-based methods such as the one used by DISSTANS also allow analytic inclusion of a priori model parameter knowledge, which may be added in future versions.

We omit a detailed look here at hyperparameters (e.g., regularization penalties, the number of iterations), as differing goals, as well as different characteristics of the data, will have a large impact on what the "best" choice is, and general assertions are therefore not possible. The tools presented here therefore do not relieve the user of the task of finding the best set of hyperparameters for their data and problem formulation, although the documentation includes the specific choices for the cases presented in the previous section (based on both analytic and empirical considerations), which may provide a good starting point.

An important caveat of using a fixed dictionary of splines to model transient signals is that such fits are not phase-invariant. Processes that move both in space and time (e.g., slow slip events in Cascadia, Riel et al., 2014) are "discretized" by the onset times of individual splines, such that multiple splines (of possibly different periods) are necessary to capture a potentially simple signal that migrates in time. Failing to account for different onset times throughout the network could impact the quality of fit, as well as reduce the sparsity of the solution. However, experience shows that phase invariance is not as crucial as it may seem: First, observation noise makes exact onset times of transient signals hard to determine, and simultaneously allows the solver to fit splines that are adjacent in time when the "best" onset time would be somewhere in between the splines' onset times. Second, if the problem persists, more splines of different periods or new onset times can be easily inserted into the models (with the main drawback being higher computational costs). In neither the synthetic nor real data examples presented here did the splines' periods or onset times have to be adjusted from an initial, default configuration to obtain a high-quality decomposition.

6. Conclusion

Displacement timeseries of regional GNSS networks are commonly used to monitor surface deformation, plate motion, as well as transient signals such as hydrological loading or aseismic slip events. A crucial step in these analyses is the decomposition of the input (raw) timeseries into its constituents: secular motion, periodic seasonal variations, step offsets due to earthquakes, etc. As networks continue to grow in number and size, so does the need to efficiently analyze timeseries. We combine the many features of previously published analysis methods into a single, generic, open-source framework. The DISSTANS Python package includes: (1) incorporation of spatial information through the use of a spatial L0-regularized least-squares solver, (2) CPU-based parallelization for scaling to large networks, (3) formal uncertainty quantification with covariance matrices between components and constituents, (4) a suite of supporting tools including timeseries files data management, common mode estimation, and simple, automated step detection, as well as (5) visualization methods to accelerate data and model inspection by the user.

Validation with synthetic GNSS network timeseries shows the beneficial effect of fitting transient signals with the spatial, L0-regularized solver: transients in the data are fit sparsely both in time and space, and are able to recover the true underlying motion better than comparable solutions without spatial awareness. An analysis of GNSS displacement timeseries from the Long Valley Caldera region in the Sierra Nevada, California, USA demonstrates the viability of our approach using real data, jointly decomposing the timeseries into step offsets, secular motion, transient signals, as well as time-varying seasonal displacements.

Computer Code Availability

DISSTANS is available at `https://github.com/tobiscode/disstans` under the GPL-3.0 License.

Acknowledgements

This work has been partially supported through a collaboration with the King Abdulaziz City for Science and Technology (KACST).

CRediT authorship contribution statement

Tobias Köhne: Methodology, Software, Validation, Writing: Original Draft, Visualization. **Bryan Riel:** Methodology, Writing: Review & Editing. **Mark Simons:** Conceptualization, Resources, Writing: Review & Editing, Supervision, Funding acquisition.

A. Key Implementation Details

DISSTANS is written in Python. While the main text reports results obtained with DISSTANS, we focus here

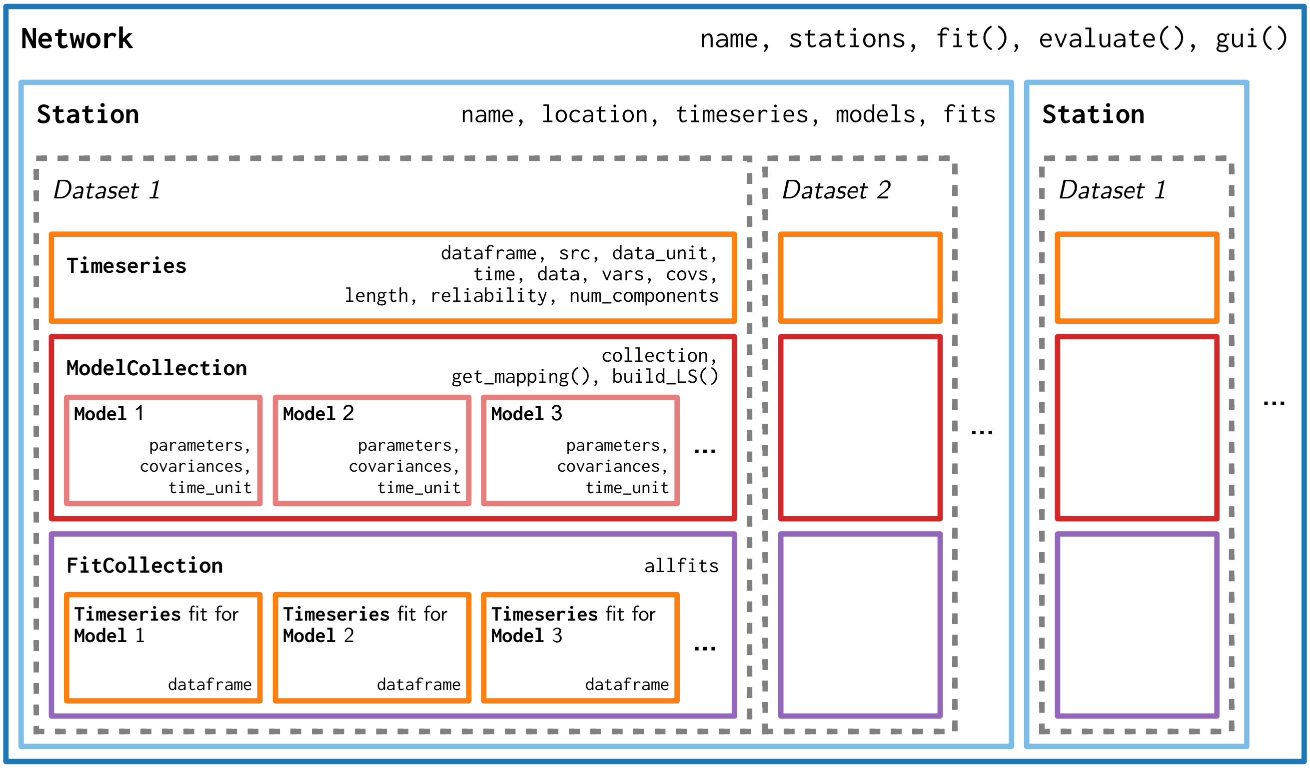

Figure A1: Code structure of DISSTANS, explained in detail in Appendix A.1.

on presenting the structure and methodology of the package, with little to no actual sample code. For sample code, please refer to the package documentation. The following typesetting will be used for clarity: classes are capitalized and typeset in bold monospace font (e.g., **`Station`**) and attributes, properties, variables, methods, functions as well as general code are typeset in regular monospace font (e.g., `parameters` or `import disstans`) with callables (e.g., functions and methods) additionally being trailed with parentheses (e.g., `get_mapping()`).

A.1. Structure

Fig. A1 presents the modular structure of DISSTANS. The highest level of abstraction is the **`Network`** class, which serves three main purposes. First, for each station in the network, it contains a **`Station`** object in its `stations` dictionary attribute, which enables straightforward access. Its second use is to provide a suite of convenience methods that perform a certain task for each station. Without parallelization enabled, their only advantage is that a user does not have to write explicit for-loops. However, **`Network`** methods also implement an automatic switch to parallelized execution using Python's `multiprocessing.pool` module if the configuration is set accordingly. Finally, the **`Network`** class contains methods that interface with all stations simultaneously; for example, the graphical user interface `gui()` and other plotting functions (more details about visualization methods in Appendix A.8). Plotting functions are based on the standard Matplotlib (Hunter, 2007) and Cartopy (Elson et al., 2022) packages.

One level down in the hierarchy is the **`Station`** class. Apart from storing the metadata information `name` and `location`, it is the container object for all datasets being assigned to the station; for example, raw or post-processed GNSS displacement timeseries (e.g., *Dataset 1* and *Dataset 2* in Fig. A1). A network can contain multiple stations, and each station can contain multiple datasets, but not all datasets have to be present at all stations. The **`Station`** class also provides functions that directly work on contained timeseries, such as `analyze_residuals()`.

On the third level, for each dataset, a station contains three key elements: the actual data (in the **`Timeseries`** object, stored in the `Station.timeseries` dictionary), the associated models (as a **`ModelCollection`** object containing the individual **`Model`** objects, stored in the `Station.models` dictionary), and any fits to the data based on model evaluations (as a dictionary of **`Timeseries`** objects, one for each model, plus one for all models jointly, all stored in the `Station.fits` **`FitCollection`** object). Using the methods provided by the **`Station`** class ensures that whenever a new dataset is added (or removed), all three elements are initialized (or deleted) appropriately. While this separation might appear somewhat confusing, it is necessary to enable easy access to individual objects while preserving flexibility. For example, a **`Timeseries`** object is physically independent of whatever model one wants to apply to it, and therefore the code should reflect this (i.e., the **`Timeseries`** object should not change when a model is added or removed, or when an individual model is evaluated to yield a prediction). The separation into data, models, and fits also allows for the same dataset to easily have different models at different stations, or multiple models of the same class (e.g., two sets of step functions, one for maintenance and one for earthquake-induced steps). Using the **`Timeseries`** class also for fits (i.e., model-predicted timeseries) allows for the efficient re-use of practical **`Timeseries`** methods such as file storage or mathematical operations.

On the lowest level, the **`Model`** and **`Timeseries`** objects store their data using standard NumPy arrays (Harris et al., 2020) and pandas DataFrames (McKinney, 2010; The pandas development team, 2021), respectively, enabling seamless integration with existing Python-based workflows.

The open-source nature of the code, along with a defined hierarchical, object-oriented structure, allows for easy modification and extension by the user through subclassing. For example, storing additional station metadata such as antenna information can easily be implemented by creating a Python class inheriting from the **`Station`** class and extending the initialization function to accept additional instance variables. Another example is the implementation of new user-defined models by subclassing **`Model`** which then seamlessly integrate into the rest of DISSTANS's workflow. Finally, loading timeseries data from a custom data format can be integrated into DISSTANS by subclassing the **`Timeseries`** class. In fact, all of the included models (see below) and timeseries file formats are subclasses of **`Model`** and **`Timeseries`**, respectively, and can be used as examples by users wishing to extend the code functionality.

A.2. Models

DISSTANS uses a linear combination of parametric models. Parametric models linear in their coefficients (i.e., not necessarily composed of linear functions) allow both simple unregularized as well as more complex L2, L1 or L0 regularized least-squares fitting (more detail about regularization schemes in Appendix A.3). Furthermore, estimating multiple models jointly is straightforward as they are linearly added together, and the mapping (or design) matrix is simply a horizontal stack of all the models' individual mapping matrices (everything automatically done by the **`ModelCollection`** class). Lastly, the formal estimated model parameter covariance matrix can usually be estimated in closed-form.

The individual **`Model`** classes included in DISSTANS can be separated into basic and spline models. All models can be used with one or multiple data components. The basic models currently included are: **`Polynomial`**, **`Step`**, **`Sinusoid`**, **`Logarithmic`**, **`Exponential`**, **`HyperbolicTangent`** and **`Arctangent`**. The basic models are either single functions (e.g., logarithm), or their functions form orthogonal bases within their class (e.g., polynomials). The spline modeling in **`BSpline`** or **`ISpline`** model is based on Hetland et al. (2012) and Riel et al. (2014), containing multiple cardinal B- or integrated-B-splines (respectively) of the same timescale and order but with different center times. The **`SplineSet`** combines several **`BSpline`** or **`ISpline`** models of different timescales into one large collection, forming a linearly-dependent (overcomplete) spanning set able to approximate arbitrary functions. The **`AmpPhModulatedSinusoid`** estimates a sinusoid of a given nominal frequency, but allows the instantaneous amplitude and phase to vary. Time-varying properties are enabled by modeling the linear sine and cosine coefficients of the sinusoid as being defined by a linearly-independent set of B-Spline basis functions over the given time interval. Some form of regularization is necessary to gain a meaningful result when using an overcomplete set of splines.

A.2.1. Joint Mathematical Formulation

In DISSTANS, the joint mathematical formulation $g(t)$ is the sum of all the individual models contained in a **`ModelCollection`**. Each individual constituent $g_{\texttt{Model}}$ (described by **`Model`** objects) can again be a linear superposition of functions g_j and corresponding coefficients m_j:

$$g(t) = \sum g_{\texttt{Model}}(t) \tag{1a}$$

$$= \sum_{j=1}^{\texttt{num\_parameters}} m_j g_j(t) \tag{1b}$$

Here, `num_parameters` is the total number of all individual functions, and therefore also the number of all coefficients to be estimated.

While the models are continuous in time, timeseries decomposition inherently works on discrete observations d_i at times t_i. Using matrix notation, the least-squares problem can be formulated as follows:

$$\mathbf{d} = \mathbf{G}\mathbf{m} + \epsilon \tag{2}$$

Where

$$\mathbf{d} = \left(d_i\right) \in \mathbb{R}^{\texttt{num\_observations} \times 1} \tag{3a}$$

$$\mathbf{G} = \left(G_{i,j}\right) \in \mathbb{R}^{\texttt{num\_observations} \times \texttt{num\_parameters}} \tag{3b}$$

$$= \left(g_j\left(t_i\right)\right) \in \mathbb{R}^{\texttt{num\_observations} \times \texttt{num\_parameters}} \tag{3c}$$

$$\mathbf{m} = \left(m_j\right) \in \mathbb{R}^{\texttt{num\_parameters} \times 1} \tag{3d}$$

and $\epsilon \in \mathbb{R}^{\texttt{num\_observations} \times 1}$ is the column vector of residuals. All solvers start from this formulation to find the best set of m_j that minimizes a given cost function dependent on ϵ (potentially including regularization criteria, see Appendix A.3). The choice of the data misfit loss function implicitly defines the assumed distribution from which ϵ is drawn (e.g., a Normal distribution in the case of unregularized least-squares). The observations can include measurements in all three dimensions, allowing the use of cross-component covariances in the fitting process. In DISSTANS, the mapping (i.e., design) matrices $\mathbf{G}$ are assembled by the `get_mapping()` methods, $\mathbf{d}$ is represented by **`Timeseries`** objects, and $\mathbf{m}$ is returned by the solver in **`Solution`** objects and added to each **`Model`** object.

In the following three subsections, we detail both the basic and the spline-based models.

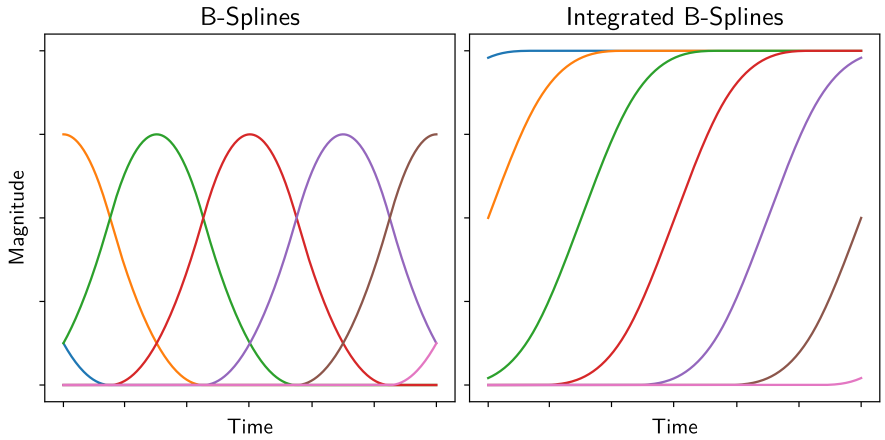

Figure A2: Example of `BSpline` (left) and `ISpline` (right) spline functions for a single timescale and order at seven different center times. Each curve on the right is the integral of the curve on the left of the same color.

A.2.2. Basic Models

The basic models in DISSTANS include function commonly used to model geodetic timeseries:

$$g_{\texttt{Arctangent}}(t) = m' \left(\frac{1}{\pi} \arctan \left(\frac{t}{\tau} \right) + 0.5 \right) \tag{4a}$$

$$g_{\texttt{Exponential}}(t) = m' \left(1 - \exp \left(-\frac{t}{\tau} \right) \right) \tag{4b}$$

$$g_{\texttt{HyperbolicTangent}}(t) = m' \left(\frac{1}{2} \tanh \left(\frac{t}{\tau} \right) + 0.5 \right) \tag{4c}$$

$$g_{\texttt{Logarithmic}}(t) = m' \log \left(1 + \frac{t}{\tau} \right) \tag{4d}$$

$$g_{\texttt{Polynomial}}(t) = \sum_{l} m'_l t^l \tag{4e}$$

$$g_{\texttt{Step}}(t) = \sum_{l} m'_l H \left(t - t_l^{\text{step}} \right) \tag{4f}$$

$$g_{\texttt{Sinusoid}}(t) = m'_0 \cos(\omega t) + m'_1 \sin(\omega t) \tag{4g}$$

where all m' are just stand-ins for the overall set of m_j, τ can vary between models, the t_l^{step} are step times, and $H(t)$ is the Heaviside function. While all of these models are available out-of-the-box, the user still has to actively specify which models to use, how many of each, and with which reference times, timescales, or periods.

A.2.3. Linearly Dependent, Overcomplete Dictionary of Splines: `SplineSet`

For study areas where significant transients of arbitrary shape can be found, DISSTANS offers spline-based transient modeling.

We start with the formulation of a single cardinal B-spline basis function (*spline function*) of reference time t_{ref}. "Normalized" timestamps t' can be calculated as follows:

$$t' = \frac{t - t_{\text{ref}}}{\rho} \tag{5}$$

By default, this single spline function is then shifted to multiple center times by using its timescale ρ, leading to different normalized timevectors for each spline function:

$$t'_j = \frac{(t - t_{\text{ref}}) - j \cdot \rho}{\rho} \tag{6}$$

(Here, $j = 0 \ldots$ `num_splines` only considers the spline functions.)

To create the spline functions of a certain degree p (with order $n = p + 1$), we can then use the following relation (Butzer et al., 1988; Schoenberg, 1973):

$$g_j(t'_j) = \sum_{k=0}^{n} \frac{(-1)^k}{p!} \cdot \binom{n}{k} \cdot \left(t'_j + \frac{n}{2} - k \right)^p \tag{7}$$

This is the model represented by `BSpline`. Based on Hetland et al. (2012), this study uses the integrated form of this spline function to represent transients. Its mathematical representation is:

$$g_j(t'_j) = \sum_{k=0}^{n} \frac{(-1)^k}{(p+1)!} \cdot \binom{n}{k} \cdot \left(t'_j + \frac{n}{2} - k \right)^{p+1} \tag{8}$$

The final spline model (a single `BSpline` or `ISpline` object) over all the available center times is therefore

$$g_{\texttt{\{B,I\}Spline}}(t) = \sum_{j=0}^{\texttt{num\_splines}} m_j g_j(t) \tag{9}$$

Within the `SplineSet` class, this model can then be repeated again for different timescales ρ. Fig. A2 shows example spline functions.

A.2.4. Linearly Independent Spline Basis for Time-varying Sinusoids: `AmpPhModulatedSinusoid`

For study areas where the amplitude of seasonal oscillations varies significantly, DISSTANS offers varying-amplitude sinusoidal modeling. Such modeling can also be used to improve the fitting of shortterm transient processes, as potentially periodic parts can then be accommodated by the seasonal model.

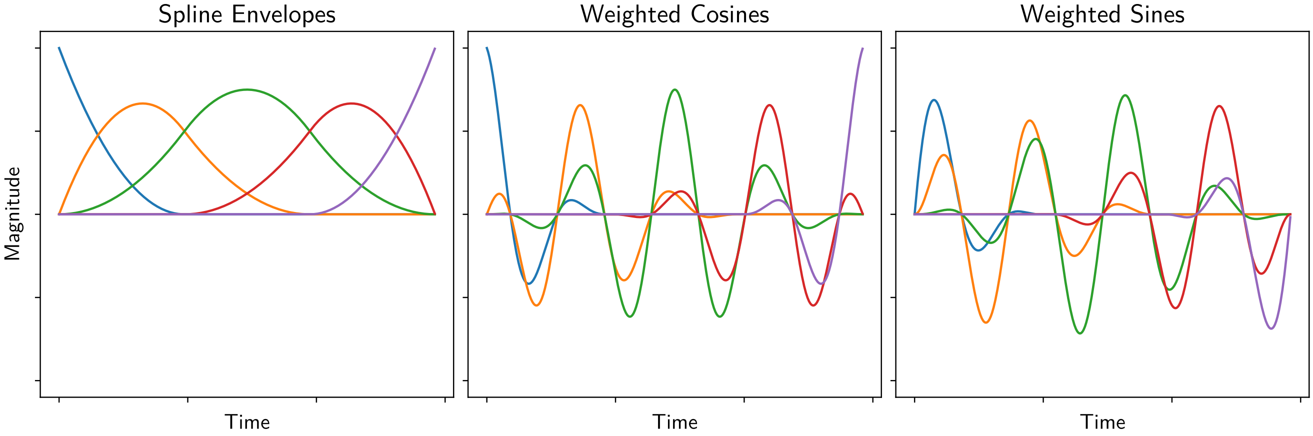

Figure A3: Visualization of the intermediate functions used by `AmpPhModulatedSinusoid`. The spline basis functions h_j over the considered time interval are in the left panel. Multiplying the spline functions with the cosine and sine of a given period then yields the modulated cosines and sines in the center and right panel, respectively.

The simple `Sinusoid` class models a seasonal signal, given a certain frequency ω, as the linear combination of a sine and cosine combination, allowing one to estimate both phase ϕ and amplitude A as a linear problem:

$$g_{\texttt{Sinusoid}}(t) = A\cos(\omega t - \phi) = a\cos(\omega t) + b\sin(\omega t) \quad (10)$$

If we want to allow the overall amplitude A to change over time, we can extend the definition of a (and similarly, b):

$$a \rightarrow a(t) = \bar{a} + \Delta a(t) \quad (11a)$$

$$b \rightarrow b(t) = \bar{b} + \Delta b(t) \quad (11b)$$

To keep the problem linear, we can use a spline representation for $\Delta a(t)$, $\Delta b(t)$:

$$a(t) = \bar{a} + \sum_j a_j h_j(t) \quad (12a)$$

$$b(t) = \bar{b} + \sum_j b_j h_j(t) \quad (12b)$$

Where the a_j (and respectively, b_j) are the parameters m_j to estimate, and h_j are the spline basis functions (more on h_j below). Expanding $g_{\texttt{Sinusoid}}(t)$ with the extended definition leads to a natural separation of components:

$$\begin{aligned}
& a(t)\cos(\omega t) + b(t)\sin(\omega t) \\
=\; & (\bar{a} + \Delta a(t))\cos(\omega t) \\
& + \left(\bar{b} + \Delta b(t)\right)\sin(\omega t) \\
=\; & \left(\bar{a}\cos(\omega t) + \bar{b}\sin(\omega t)\right) \\
& + (\Delta a(t)\cos(\omega t) + \Delta b(t)\sin(\omega t)) \qquad (13) \\
=\; & \left(\bar{a}\cos(\omega t) + \bar{b}\sin(\omega t)\right) \\
& + \sum_j \left(a_j h_j(t)\cos(\omega t) + b_j h_j(t)\sin(\omega t)\right) \\
=\; & g_{\texttt{Sinusoid}}(t) + g_{\texttt{AmpPhModulatedSinusoid}}(t)
\end{aligned}$$

Here, the first term represents the *nominal* component, and the second term the *deviation* component. In DISSTANS, the terms correspond to the `Sinusoid` and `AmpPhModulatedSinusoid`, respectively.

Note that the h_j are not the same as for the dictionary of splines defined above. The dictionary is comprised of a single (cardinal) spline, that is of a defined length scale (i.e., period), and centered at specified timestamps. Here, for `AmpPhModulatedSinusoid`, we do not need the spline to be the same one shifted and scaled, instead we can default to the more general notion of B-Splines — a complete basis for polynomials of a given degree on a given interval. This relaxation allows us to use SciPy's basis function implementation directly (Virtanen et al., 2020). Fig. A3 shows an example set of spline basis functions h_j, as well as the resulting modulated cosine and sine terms used as the spanning functions for `AmpPhModulatedSinusoid`.

Although it is not strictly necessary to include $\bar{a}$ and $\bar{b}$ explicitly in $a(t)$ and $b(t)$ (splines can also represent any constant function), the separation is useful because it allows a regularized solver to not penalize the nominal component.

A.3. Solver Functions

The provided solver functions are least-squares (therefore parametric) solvers, with varying degrees of added complexity. They each

1. Build the mapping and observation matrices for a given `Timeseries` object of observations and `ModelCollection` object ($\mathbf{G}$ and $\mathbf{d}$, respectively, see Appendix A.2),
2. Divide the solution process into independent subproblems if there is no data component covariance (decreasing the computational burden),
3. Call a lower-level solver to minimize the cost function $\|\mathbf{Gm} - \mathbf{d}\|_2^2$ (potentially subject to regularization),
4. Optionally calculate the formal model parameter covariance matrix $\mathbf{C}_m$, and
5. Return a `Solution` object (containing the best-fitting $\mathbf{m}$).

To prevent convergence or numerical issues, the solvers and the **`Solution`** class keep track of model parameters that cannot be estimated (because they are not observable given the timespan of the observations) or should not be estimated (useful, for example, if some splines in a **`SplineSet`** are assumed to be zero). The regularized solvers additionally keep track of which model's parameters should be regularized, allowing for a flexible regularization approach.

The first, most basic solver is `linear_regression()`, which provides the above-mentioned features as a wrapper to the least-squares routine in SciPy (Virtanen et al., 2020). It can therefore be regarded as a minimal code example for new, user-defined solvers. The cost function to be minimized is:

$$\|\mathbf{Gm} - \mathbf{d}\|_2^2 \tag{14}$$

and the posterior covariance matrix $\mathbf{C}_m$ given the data covariance matrix $\mathbf{C}_d$ is

$$\mathbf{C}_m = \left(\mathbf{G}^T \mathbf{C}_d^{-1} \mathbf{G}\right)^{-1} \tag{15}$$

where $^{-1}$ is the generalized pseudo-inverse for matrices.

The second provided solver, `ridge_regression()`, adds L2 regularization, and also relies on the least-squares routine in SciPy. It minimizes the cost function

$$\|\mathbf{Gm} - \mathbf{d}\|_2^2 + \lambda \|\mathbf{m}_{\text{reg}}\|_2^2 \tag{16}$$

where λ is a chosen regularization penalty hyperparameter, and $\mathbf{m}_{\text{reg}}$ is the subset of $\mathbf{m}$ that should be regularized. Furthermore, λ can vary between data components to account for different noise levels. The posterior covariance matrix takes the regularization into account:

$$\mathbf{C}_m = \left(\mathbf{G}^T \mathbf{C}_d^{-1} \mathbf{G} + \lambda \mathbf{I}_{\text{reg}}\right)^{-1} \tag{17}$$

The third solver, `lasso_regression()`, uses CVXPY (Diamond and Boyd, 2016; Agrawal et al., 2018) to provide L1 and, by means of weighted iterations, station-specific L0 regularization (Candès et al., 2008). In its basic form, the solver minimizes

$$\|\mathbf{Gm} - \mathbf{d}\|_2^2 + \lambda \|\mathbf{m}_{\text{reg}}\|_1 \tag{18}$$

By defining a reweighting function and iterating on the L1-regularized solution, the `lasso_regression()` solver approximates the solution for the L0-regularized[3] least-squares problem, minimizing

$$\|\mathbf{Gm} - \mathbf{d}\|_2^2 + \|\mathbf{m}_{\text{reg}}\|_0 \tag{19}$$

Because the result of an L0-regularized solution is approximately the same as if an unregularized problem was solved with only a subset of model parameters to be estimated, the posterior covariance matrix for `lasso_regression()` is the same as for `linear_regression()`, but setting to zero the covariances which were not estimated.

Note that the reweighting function does not explicitly appear in the L0 cost function, although it does mimic the role of the regularization penalty λ from the L2 and L1 cost functions. Specifically, during the iteration process, the reweighting function returns penalties that anticorrelate with parameter amplitude: small parameters will be penalized heavily, and large parameters will receive very little penalty. With this approach, the solver converges to the L0-regularized solution where parameters either have near-zero penalty (if the parameters are deemed significant by the solver), or near-zero amplitude (because of their high penalty). Consequently, the final cost function does not contain an explicit penalty hyperparameter λ, although care needs to be taken when specifying the reweighting function such that it is able to distinguish insignificant from significant parameters. Thresholds for this distinction are not hard cut-offs; they are defined within the context of **`ReweightingFunction`** objects, and usually correspond to the location of an L-shape bend in the reweighting function's shape. While the appropriate choice of functions and scales will vary between applications, a good (empirical) starting point are functions whose penalties close to an input value of zero are of a similar order of magnitude of the data being fitted. For more details about the implementation of the L0-regularized solver, including examples of reweighting functions, see Candès et al. (2008).

The `Network.spatialfit()` method extends the possibilities of station-specific L0 regularization to also take into account the weights of a given model at nearby stations. The approach implemented here follows Riel et al. (2014) closely, with the goal to identify signals close to the noise floor, suppress local noise, and promote sparse models in both time *and* space. A visual summary of the method is given in Fig. A4. DISSTANS is able to perform the station-specific fits in parallel, resulting in a large runtime improvement. Lastly, `Network.spatialfit()` can also minimize the jointly L1- and L0-regularized problem:

$$\|\mathbf{Gm} - \mathbf{d}\|_2^2 + \lambda \|\mathbf{m}_{\text{reg,L1}}\|_1 + \|\mathbf{m}_{\text{reg,L0}}\|_0 \tag{20}$$

A.4. Data Formats

All timeseries datasets are stored as objects of **`Timeseries`** subclasses. The **`Timeseries`** parent class defines an internal data structure that all further processing done by DISSTANS methods of all levels rely on. DISSTANS also implements properties such as the calculation of a timeseries length or reliability, the possibility to use Python's in-built mathematical operators to create new timeseries, and convenience functions such as cutting the timeseries or building covariance matrices at a particular timestep.

Subclasses, in turn, define how any particular input file gets loaded to match the common structure. The two provided subclasses are **`GipsyTimeseries`** (for JPL's GipsyX `.tseries` files) and **`UNRTimeseries`** (for UNR's `.tenv3` files). User-defined classes can easily be created by adhering to the format of the two existing subclasses, and checking the documentation of **`Timeseries`**.

---

[3] Here, we use the definition of Candès et al. (2008): $\|\mathbf{x}\|_0 = |\{i : x_i \neq 0\}|$, i.e., the number of non-zero elements.

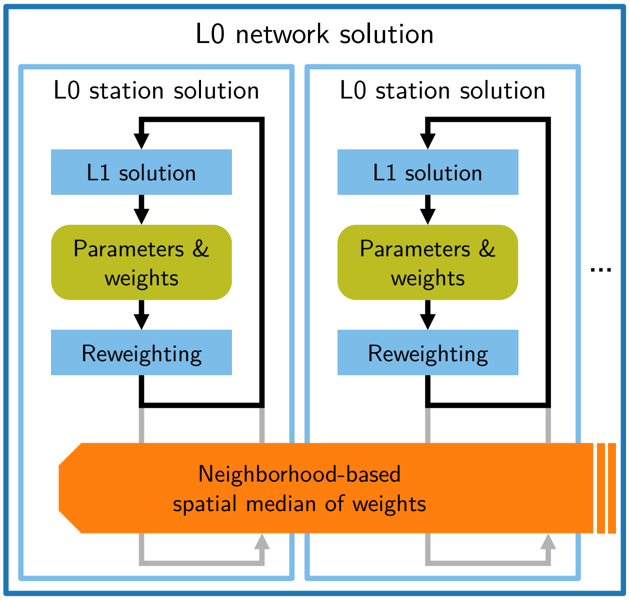

Figure A4: Flowchart of the spatiotemporal L0-regularized solver as described in Riel et al. (2014). Symbols and colors from Fig. A5. At each station, an L1-regularized least-squares fit is computed, where each parameter has an associated weight. The weight is inversely correlated to the parameter magnitude. Parameters close to zero are iteratively penalized, whereas significant parameters have their penalty gradually reduced to zero. Iterated L1 regularization effectively approximates an L0-regularized solution (see Candès et al., 2008). By combining the weights between stations with a median in an intermediate step, parameters that are significant at other nearby stations as well are promoted, and parameters that are insignificant are demoted.

A.5. Synthetic Data

The creation of synthetic data is another feature directly integrated into DISSTANS. Each **`Model`** and **`ModelCollection`** object has the two methods `read_parameters()` and `evaluate()`, which integrate into existing Python workflow by accepting and returning (respectively) NumPy arrays. A typical workflow to generate datasets therefore is to instantiate **`Model`** objects (e.g., a polynomial of a certain order), define and read in the parameters of the model, and finally evaluate the individual models (or a **`ModelCollection`** containing the individual ones). If the data is then to be used within DISSTANS, a simple **`Timeseries`** constructor exists for NumPy arrays, otherwise one can use the regular NumPy methods for exporting the data.

A.6. Step Detector

DISSTANS includes the **`StepDetector`** class to perform statistics-based assessments on whether step models should be added to a timeseries to estimate offsets due to physical (e.g., earthquakes) or non-physical (e.g., maintenance events) processes. Since there is no fully-automated algorithm that approaches the performance of manual inspection (e.g., Gazeaux et al., 2013), the focus here lies on providing a semi-automated method that is to be used in conjunction with end-user interaction. The method implemented in DISSTANS is based on the Akaike Information Criterion (AIC, e.g., Burnham and Anderson, 2002). For a given window size, the algorithm will evaluate the residuals of fitting the timeseries with two different models: one with a simple linear slope and offset, and the other with a linear slope, offset, and an additional offset in the center of the window. Then, for each timestep, the relative probability of the step versus the no-step model being true is calculated. In the last step, the maxima of the step probabilities are calculated and thresholded. The user can then examine the steps (alongside their respective variance reductions) and determine whether to add the offsets as steps to be estimated.

Our step detector approach is similar to the one in GipsyX (Bertiger et al., 2020), but where GipsyX considers multiple window sizes, DISSTANS only uses a single one. Of course, **`StepDetector`** can be run multiple times with different window sizes, such that their combined results can provide a more robust step probability estimate.

A.7. Example Workflow

Even though DISSTANS is modular and therefore highly flexible, we propose the workflow presented in Fig. A5 as a general starting point for timeseries decomposition with DISSTANS.

The first step is the acquisition and preparation of the raw input datasets, i.e., the GNSS network station displacement timeseries (and, if available, associated maintenance and seismic catalogs). Applying quality metrics such as requiring a minimum number of observations or station reliability (through their respective **`Timeseries`** attributes `num_observations` and `reliability`) ensures that the fitting process is not hindered by bad data.

We view the second step as a “preprocessing” one, where we identify and remove statistical outliers and the common mode errors (CME, see Dong et al., 2006; Huang et al., 2012) from the observations (see Fig. A6 for more detail). The relevant functions are `median()`, `clean()` and `common_mode()`, which are called on the entire network (respecting parallelization) through the **`Network`** methods `call_func_ts_return()` and `call_func_no_return()`. The CME is systematic for the entire network, reflects noise in the estimation of the reference frame and manifests itself as a high-frequency noise realization that should be estimated independently of model fits (which could create additional systematic errors). To estimate the CME (e.g., using PCA/ICA), we first remove empirically the potentially interesting, low-frequency signal using a low-pass running median. A median filter is robust when handling large steps in the data (which may be present before any step removal is performed). Outlier removal is performed on the residual between low-pass and input signal, based on the residual’s variance.

Offsets (or steps) in the data are the big obstacles for model fitting. Left unaccounted for, they will influence every other model component (e.g., the secular plate velocity).

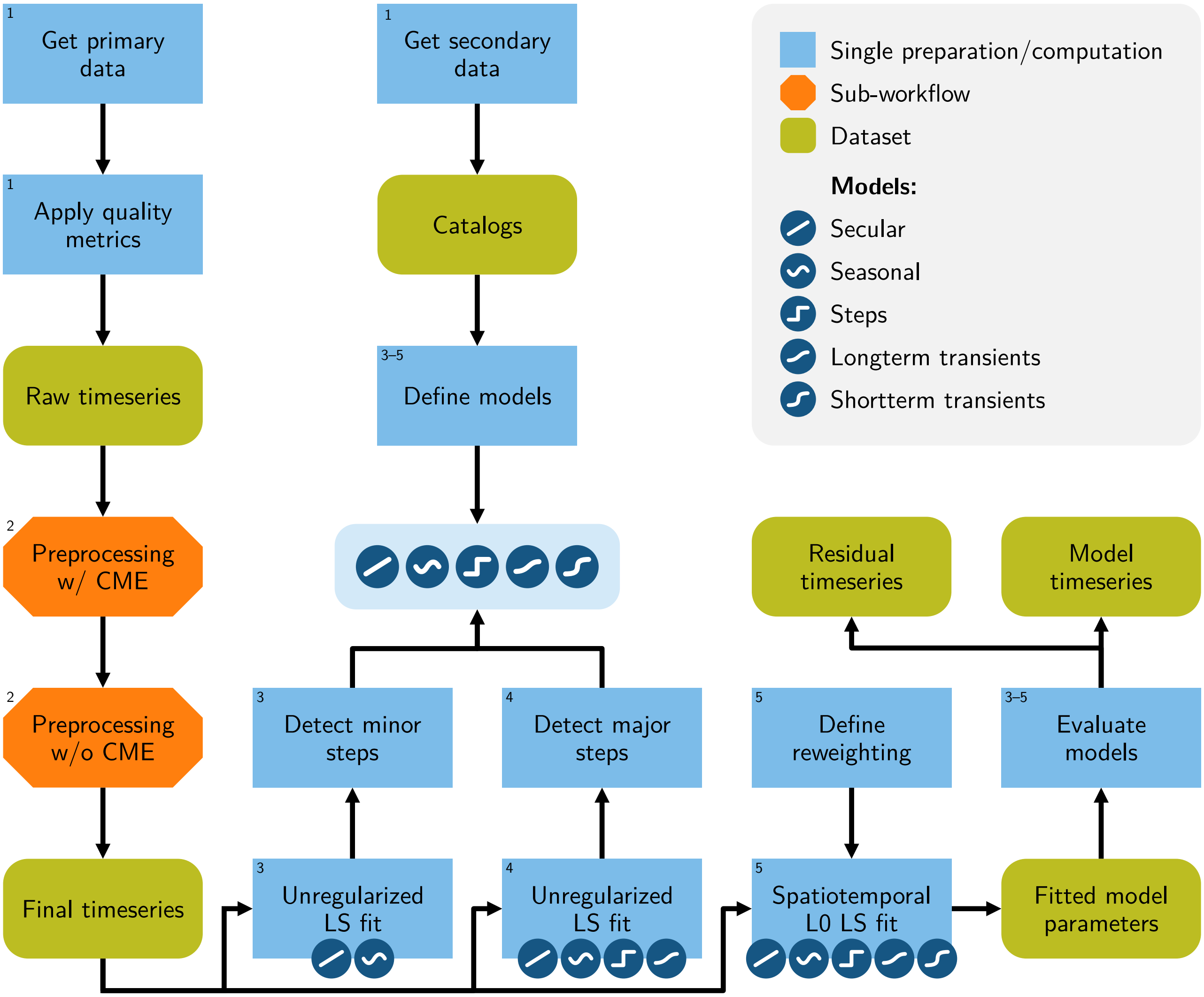

Figure A5: Example workflow for using DISSTANS, explained in detail in Appendix A.7. Blue rectangles represent single computational steps, orange rectangles with cut corners represent sub-workflows discussed in more detail elsewhere, and green, rounded rectangles represent datasets at their different stages of processing. The numbered steps in the text correspond to the numbering in the top left corners of the rectangles.

While big jumps in the data can easily be spotted by comparing a measurement with the variance around the mean of previous observations, smaller offsets that are either below or similar to the data variance, and/or are accompanied by transient motion, are more challenging to detect. Ideally, all occuring offsets are known in advance based on ancillary catalogs, and could be categorized into equipment changes and physical processes.

Maintenance events (e.g., antenna replacements, software changes, receiver upgrades) usually are well-recorded and accessible. Functions like `parse_maintenance_table()` and `parse_unr_steps()` are useful for these purposes. However, not all maintenance events automatically have a visible effect in the data, and therefore there are “grey zones” where the addition of a modeled step may be more harmful than beneficial. In these cases, we can perform an iterative process between fitting larger signals, and then checking again for evidence of smaller offsets.

A similar case can be made for the presence of coseismic displacements. Large, nearby earthquakes produce offsets that can be predicted from seismic catalogs and simple forward modeling of the expected displacement at any given station. (The `earthquakes` module provides this functionality in DISSTANS.) However, smaller events might not necessarily warrant an additional modeled step, and very fast transients would be better fit by transient models. Therefore, we recommend an iterative approach here as well.

The next steps in the proposed workflow are iterations of step-detection and model-fitting. In the third step, an unregularized least-squares fit with only a polynomial and some sinusoidal models is performed at each station individually. Using the **`StepDetector`** class, extremely prominent offsets in

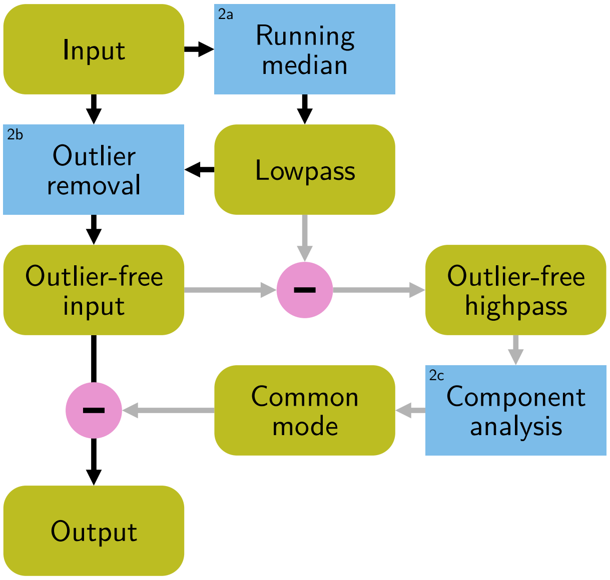

Figure A6: Preprocessing sub-workflow, following the same symbolic and coloring as Fig. A5 (step 2), with rose circles representing mathematical operations. First, a running median of the input is calculated, which results in a lowpass filtered timeseries. The variance of the input around the lowpass timeseries is used to detect outliers. Removing them from the input yields the outlier-free input. Without common mode estimation, this is also the final output. To remove the common mode, the difference between the lowpassed input and the outlier-free input is calculated, which yields an outlier-free, highpassed input. The dominant component of this timeseries is the best estimate of the common mode error. Removing this from the outlier-free input yields the outlier-free, common-mode-removed output.

the data are well resolved, and are added to a list of offsets to be fit (with the **`Step`** model class).

In the fourth step, using the initial simple models, the defined list of offsets, and a **`SplineSet`** dictionary of longterm transient splines, another unregularized least-squares fit is computed. Together with external maintenance and seismic catalogs, a second run of the **`StepDetector`** then aims to identify smaller steps that are to be estimated.

For the fifth step of the proposed workflow, the `Network.spatialfit()` method is used to perform a network-wide fit using the aforementioned polynomial, sinusoidal, and step models, as well as an expanded spline dictionary that includes also shorter-term transients. Only the spline parameters are subject to the spatiotemporal L0 regularization, although the regularization can be extended to all models. Defining an appropriate **`ReweightingFunction`** ensures a sparse, yet well-fitting solution. When seasonal effects are found to be strongly varying in time, allowing the seasonal signal to vary in amplitude over time (using **`AmpPhModulatedSinusoid`** models), can also improve the fit.

The results at each step are a set of model parameters for each data component, together with a complete parameter covariance matrix. They can be evaluated at all stages to yield the overall model-predicted timeseries (including its predicted uncertainty), as well as the individual constituent contributions. The residuals can be computed using the `Network.math()` methods and analyzed using the `Network.gui()` method to assure no systematic misfit is present. Of course, there are many variations to this example workflow.

A.8. Visualization

Because the raw data contained within **`Timeseries`** objects are standard pandas DataFrames, they can be plotted using standard Matplotlib code using their `Timeseries.time` and `Timeseries.data` attributes. Utilizing commonly-used Python object formats enables easy inspections of a particular station, timeseries, or fit; and allows for non-standard user-desired plotting. Model parameter values and covariances (accessed through their `Model.parameters` and `Model.covariances` NumPy array attributes) are also directly plottable with Matplotlib.

There are high-level visualization routines already included in DISSTANS. The core functionality is contained within the `Network.gui()` method, which provides a clickable map of the network (optionally with satellite imagery background), and a separate figure with all the timeseries contained by a station. If a timeseries contains fitted models, the overall model prediction is plotted, and optionally, can be split up into the different model components, and if there are **`SplineSet`** models present at a station, a scalogram can be shown. All figures can also be saved directly to files.

Furthermore, to visualize station motion in a map view, the `Network.wormplot()` method can produce still maps and animated videos of station displacements (or individual model constituents of them). Lastly, the `Network.graphical_cme()` method performs common mode estimation (see Appendix A.7) and presents the temporal and spatial components separately for validation purposes.

References

Agrawal, A., Verschueren, R., Diamond, S., Boyd, S., 2018. A rewriting system for convex optimization problems. Journal of Control and Decision 5, 42–60. doi:10.1080/23307706.2017.1397554.

Altamimi, Z., Métivier, L., Rebischung, P., Rouby, H., Collilieux, X., 2017. ITRF2014 plate motion model. Geophysical Journal International 209, 1906–1912. doi:10.1093/gji/ggx136.

Bedford, J., Bevis, M., 2018. Greedy Automatic Signal Decomposition and Its Application to Daily GPS Time Series. Journal of Geophysical Research: Solid Earth 123, 6992–7003. doi:10.1029/2017JB014765.

Bekaert, D.P.S., Segall, P., Wright, T.J., Hooper, A.J., 2016. A Network Inversion Filter combining GNSS and InSAR for tectonic slip modeling. Journal of Geophysical Research: Solid Earth 121, 2069–2086. doi:10.1002/2015JB012638.

Bertiger, W., Bar-Sever, Y., Dorsey, A., Haines, B., Harvey, N., Hemberger, D., Heflin, M., Lu, W., Miller, M., Moore, A.W., Murphy, D., Ries, P., Romans, L., Sibois, A., Sibthorpe, A., Szilagyi, B., Vallisneri, M., Willis, P., 2020. GipsyX/RTGx, a new tool set for space geodetic operations and research. Advances in Space Research 66, 469–489. doi:10.1016/j.asr.2020.04.015.

Blewitt, G., 2015. GPS and Space-Based Geodetic Methods, in: Schubert, G. (Ed.), Treatise on Geophysics (Second Edition). Elsevier, Oxford, pp. 307–338. doi:10.1016/B978-0-444-53802-4.00060-9.

Blewitt, G., Hammond, W., Kreemer, C., 2018. Harnessing the GPS Data Explosion for Interdisciplinary Science. Eos 99. doi:10.1029/2018EO104623.

Blewitt, G., Kreemer, C., Hammond, W.C., Gazeaux, J., 2016. MIDAS robust trend estimator for accurate GPS station velocities without step detection. Journal of Geophysical Research: Solid Earth 121, 2054–2068. doi:10.1002/2015JB012552.

Burnham, K.P., Anderson, D.R., 2002. Information and Likelihood Theory: A Basis for Model Selection and Inference, in: Model Selection and Multimodel Inference: A Practical Information-Theoretic Approach. Springer, New York, NY, pp. 49–97. doi:10.1007/978-0-387-22456-5_2.

Butzer, P.L., Schmidt, M., Stark, E.L., 1988. Observations on the History of Central B-Splines. Archive for History of Exact Sciences 39, 137–156.

Candès, E.J., Wakin, M.B., Boyd, S.P., 2008. Enhancing Sparsity by Reweighted $\ell 1$ Minimization. Journal of Fourier Analysis and Applications 14, 877–905. doi:10.1007/s00041-008-9045-x.

Diamond, S., Boyd, S., 2016. CVXPY: A Python-Embedded Modeling Language for Convex Optimization. Journal of machine learning research: JMLR 17, 83.

Dong, D., Fang, P., Bock, Y., Webb, F., Prawirodirdjo, L., Kedar, S., Jamason, P., 2006. Spatiotemporal filtering using principal component analysis and Karhunen-Loeve expansion approaches for regional GPS network analysis. Journal of Geophysical Research: Solid Earth 111. doi:10.1029/2005JB003806.

Dong, D., Herring, T.A., King, R.W., 1998. Estimating regional deformation from a combination of space and terrestrial geodetic data. Journal of Geodesy 72, 200–214. doi:10.1007/s001900050161.

Elson, P., de Andrade, E.S., Lucas, G., May, R., Hattersley, R., Campbell, E., Dawson, A., Raynaud, S., scmc72, Little, B., Snow, A.D., Donkers, K., Blay, B., Killick, P., Wilson, N., Peglar, P., lbdreyer, Andrew, Szymaniak, J., Berchet, A., Bosley, C., Davis, L., Filipe, Krasting, J., Bradbury, M., Kirkham, D., stephenworsley, Clément, Caria, G., Hedley, M., 2022. SciTools/cartopy: V0.20.2. Zenodo. doi:10.5281/zenodo.5842769.

Gazeaux, J., Williams, S., King, M., Bos, M., Dach, R., Deo, M., Moore, A.W., Ostini, L., Petrie, E., Roggero, M., Teferle, F.N., Olivares, G., Webb, F.H., 2013. Detecting offsets in GPS time series: First results from the detection of offsets in GPS experiment. Journal of Geophysical Research: Solid Earth 118, 2397–2407. doi:10.1002/jgrb.50152.

Gualandi, A., Serpelloni, E., Belardinelli, M.E., 2016. Blind source separation problem in GPS time series. Journal of Geodesy 90, 323–341. doi:10.1007/s00190-015-0875-4.

Harris, C.R., Millman, K.J., van der Walt, S.J., Gommers, R., Virtanen, P., Cournapeau, D., Wieser, E., Taylor, J., Berg, S., Smith, N.J., Kern, R., Picus, M., Hoyer, S., van Kerkwijk, M.H., Brett, M., Haldane, A., del Río, J.F., Wiebe, M., Peterson, P., Gérard-Marchant, P., Sheppard, K., Reddy, T., Weckesser, W., Abbasi, H., Gohlke, C., Oliphant, T.E., 2020. Array programming with NumPy. Nature 585, 357–362. doi:10.1038/s41586-020-2649-2.

Heflin, M., Donnellan, A., Parker, J., Lyzenga, G., Moore, A., Ludwig, L.G., Rundle, J., Wang, J., Pierce, M., 2020. Automated Estimation and Tools to Extract Positions, Velocities, Breaks, and Seasonal Terms From Daily GNSS Measurements: Illuminating Nonlinear Salton Trough Deformation. Earth and Space Science 7, e2019EA000644. doi:10.1029/2019EA000644.

Herring, T.A., King, R.W., Floyd, M.A., McClusky, S.C., 2018. Introduction to GAMIT/GLOBK. Massachusetts Institute of Technology.

Herring, T.A., Melbourne, T.I., Murray, M.H., Floyd, M.A., Szeliga, W.M., King, R.W., Phillips, D.A., Puskas, C.M., Santillan, M., Wang, L., 2016. Plate Boundary Observatory and related networks: GPS data analysis methods and geodetic products. Reviews of Geophysics 54, 759–808. doi:10.1002/2016RG000529.

Hetland, E.A., Musé, P., Simons, M., Lin, Y.N., Agram, P.S., DiCaprio, C.J., 2012. Multiscale InSAR Time Series (MInTS) analysis of surface deformation. Journal of Geophysical Research: Solid Earth 117. doi:10.1029/2011JB008731.

Houston, H., Delbridge, B.G., Wech, A.G., Creager, K.C., 2011. Rapid tremor reversals in Cascadia generated by a weakened plate interface. Nature Geoscience 4, 404–409. doi:10.1038/ngeo1157.

Hsu, Y.J., Yu, S.B., Chen, H.Y., 2009. Coseismic and postseismic deformation associated with the 2003 Chengkung, Taiwan, earthquake. Geophysical Journal International 176, 420–430. doi:10.1111/j.1365-246X.2008.04009.x.

Huang, D.W., Dai, W.J., Luo, F.X., 2012. ICA Spatiotemporal Filtering Method and Its Application in GPS Deformation Monitoring. Applied Mechanics and Materials 204–208, 2806–2812. doi:10.4028/www.scientific.net/AMM.204-208.2806.

Hunter, J.D., 2007. Matplotlib: A 2D Graphics Environment. Computing in Science Engineering 9, 90–95. doi:10.1109/MCSE.2007.55.

Ji, K.H., Herring, T.A., Llenos, A.L., 2013. Near real-time monitoring of volcanic surface deformation from GPS measurements at Long Valley Caldera, California. Geophysical Research Letters 40, 1054–1058. doi:10.1002/grl.50258.

Langbein, J., 2020. Methods for Rapidly Estimating Velocity Precision from GNSS Time Series in the Presence of Temporal Correlation: A New Method and Comparison of Existing Methods. Journal of Geophysical Research: Solid Earth 125, e2019JB019132. doi:10.1029/2019JB019132.

McGuire, J.J., Segall, P., 2003. Imaging of aseismic fault slip transients recorded by dense geodetic networks. Geophysical Journal International 155, 778–788. doi:10.1111/j.1365-246X.2003.02022.x.

McKinney, W., 2010. Data Structures for Statistical Computing in Python. Proceedings of the 9th Python in Science Conference , 56–61doi:10.25080/Majora-92bf1922-00a.

Meade, B.J., Hager, B.H., 2005. Block models of crustal motion in southern California constrained by GPS measurements. Journal of Geophysical Research: Solid Earth 110. doi:10.1029/2004JB003209.

Misra, P., Enge, P., 2010. Global Positioning System: Signals, Measurements, and Performance. Ganga-Jamuna Press, Lincoln, Mass.

Montgomery-Brown, E.K., Wicks, C.W., Cervelli, P.F., Langbein, J.O., Svarc, J.L., Shelly, D.R., Hill, D.P., Lisowski, M., 2015. Renewed inflation of Long Valley Caldera, California (2011 to 2014). Geophysical Research Letters 42, 5250–5257. doi:10.1002/2015GL064338.

Riel, B., Simons, M., Agram, P., Zhan, Z., 2014. Detecting transient signals in geodetic time series using sparse estimation techniques. Journal of Geophysical Research: Solid Earth 119, 5140–5160. doi:10.1002/2014JB011077.

Santamaría-Gómez, A., 2019. SARI: Interactive GNSS position time series analysis software. GPS Solutions 23, 52. doi:10.1007/s10291-019-0846-y.

Santamaría-Gómez, A., Ray, J., 2021. Chameleonic Noise in GPS Position Time Series. Journal of Geophysical Research: Solid Earth 126, e2020JB019541. doi:10.1029/2020JB019541.

Schoenberg, I.J., 1973. The Basis Property of B-Splines, in: Cardinal Spline Interpolation. Society for Industrial and Applied Mathematics. CBMS-NSF Regional Conference Series in Applied Mathematics, pp. 11–19. doi:10.1137/1.9781611970555.ch2.

Segall, P., Matthews, M., 1997. Time dependent inversion of geodetic data. Journal of Geophysical Research: Solid Earth 102, 22391–22409. doi:10.1029/97JB01795.

Silverii, F., Montgomery-Brown, E.K., Borsa, A.A., Barbour, A.J., 2020. Hydrologically Induced Deformation in Long Valley Caldera and Adjacent Sierra Nevada. Journal of Geophysical Research: Solid Earth 125, e2020JB019495. doi:10.1029/2020JB019495.

The pandas development team, 2021. Pandas-dev/pandas: Pandas 1.3.0. Zenodo. doi:10.5281/zenodo.5060318.

Virtanen, P., Gommers, R., Oliphant, T.E., Haberland, M., Reddy, T., Cournapeau, D., Burovski, E., Peterson, P., Weckesser, W., Bright, J., van der Walt, S.J., Brett, M., Wilson, J., Millman, K.J., Mayorov, N., Nelson, A.R.J., Jones, E., Kern, R., Larson, E., Carey, C.J., Polat, İ., Feng, Y., Moore, E.W., VanderPlas, J., Laxalde, D., Perktold, J., Cimrman, R., Henriksen, I., Quintero, E.A., Harris, C.R., Archibald, A.M., Ribeiro, A.H., Pedregosa, F., van Mulbregt, P., 2020. SciPy 1.0: Fundamental algorithms for scientific computing in Python. Nature Methods 17, 261–272. doi:10.1038/s41592-019-0686-2.

Tobias Köhne received his B.S. (2016) in Mechanical Engineering from the Technical University of Munich, Germany and his M.S. (2018) in Aerospace Engineering from the University of Texas at Austin, USA focusing on orbital mechanics. He is currently a Ph.D. candidate at the California Institute of Technology, where he is working on modern tools for geodetic timeseries analysis of large-scale, continuously-operating GNSS regional networks. At Caltech, he was also part of an investigation into how machine learning approaches can aid to extract more information out of the currently available InSAR timeseries datasets, and worked on a small study on the dynamics and origins of retrograde Jupiter Trojans.

Bryan Riel received a B.Sc. degree in 2008 and M.Sc. degree in 2010 in Aerospace Engineering from the University of Texas at Austin and a Ph.D. in Geophysics from the California Institute of Technology in 2016. His graduate research was focused on geodetic time series analysis, geophysical modeling, and inverse theory, as well as radiometric calibration of synthetic aperture radar (SAR) data and quantification of elevation errors in backscatter products. In 2016, he joined the NASA Jet Propulsion Laboratory (JPL) as a signal analysis engineer in the Radar Science and Engineering Section. In 2019, he joined the Massachusetts Institute of Technology (MIT) as a research scientist, studying glacier dynamics using geodetic data and machine learning. Dr. Riel's research interests are broad and include geodetic time series analysis and decomposition, glaciology, volcanology, machine learning, physical modeling, inverse theory, and uncertainty quantification. Dr. Riel received the National Aeronautics and Space Administration Earth and Space Sciences Fellowship in 2012.

Mark Simons received the B.Sc. degree in geophysics and space physics from the University of California at Los Angeles, Los Angeles, CA, USA, in 1989, and the Ph.D. degree in geophysics from the Massachusetts Institute of Technology, Cambridge, MA, USA, in 1996. He has been with the California Institute of Technology, Pasadena, CA, USA, since 1996, where he is currently the John W. and Herberta M. Miles Professor of Geophysics at the Seismological Laboratory, Division of Geological and Planetary Science. He is also the Chief Scientist of the Jet Propulsion Laboratory. His research interests include processes associated with the seismic cycle, migration of magma and water in the subsurface, tides, and glacial rebound; tectonics and the relationship between short and long time-scale processes; glaciology, particularly basal mechanics and ice rheology; tools and applications using space geodesy, particularly GNSS and SAR; Bayesian methods for large geophysical inverse problems; and application of space geodesy for monitoring and rapid response to natural disasters. Prof. Simons is a fellow of the American Geophysical Union.

Decomposition and Inference of Sources through Spatiotemporal Analysis of Network Signals: The DISSTANS Python Package

Supplementary Material

Tobias Köhne Bryan Riel Mark Simons

June 27, 2022

S.1 Synthetic Network

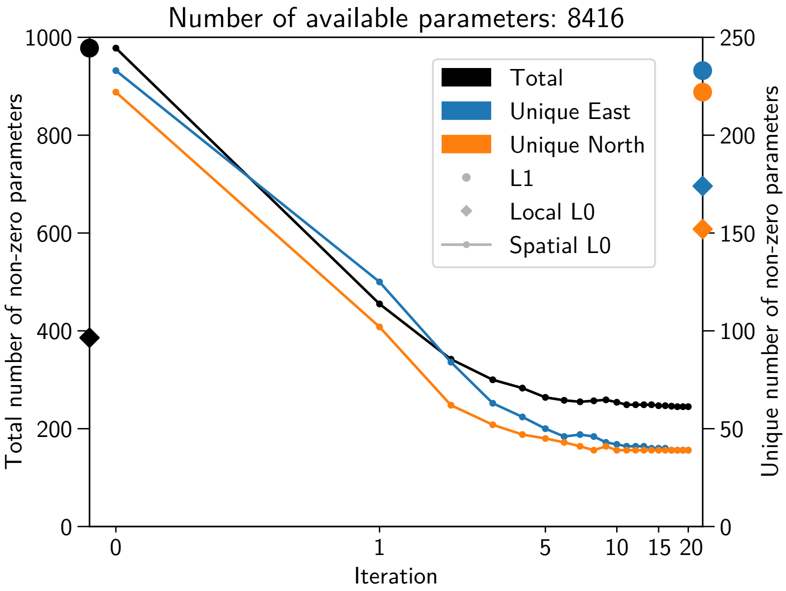

Figure S1: Convergence of the iterative, spatiotemporal L0-regularized solver (line) for 8416 total spline coefficients. For reference, values for the local L1-regularized (circles) and local L0-regularized (diamonds) solutions are also plotted on the axes. The results are shown both for the individual components (blue and orange, right vertical axis), as well as the overall solution (black, left vertical axis). The total number of non-zero parameters (i.e., the sum over all stations and components of the number of non-zero coefficients) as well as the number of *unique* non-zero parameters (i.e., the number of all splines that are non-zero at least at one station, per component) converges monotonically onto their final values. The latter number specifically demonstrates the effect of spatial sparsity.

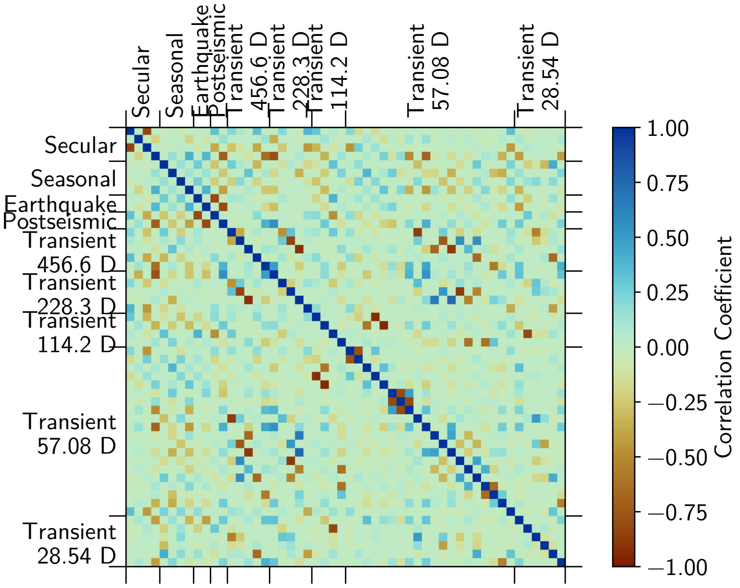

Figure S2: Model parameter correlation matrix for all models and both east-north components. The covariances for spline parameters that are estimated to be close to zero are set to zero as well, and not shown. Tradeoffs between models and within splines are clearly identifiable.

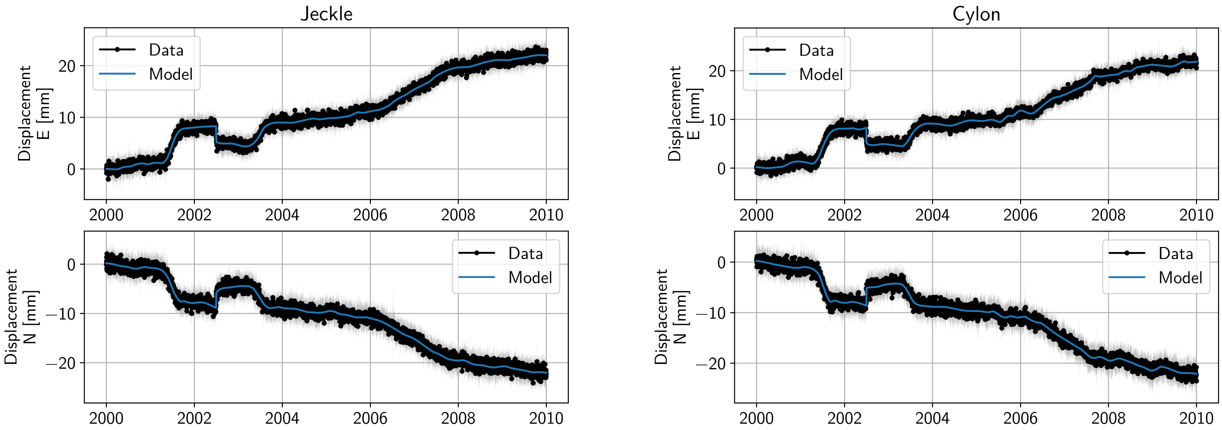

(a) Jeckle, L1 **(b)** Cylon, L1

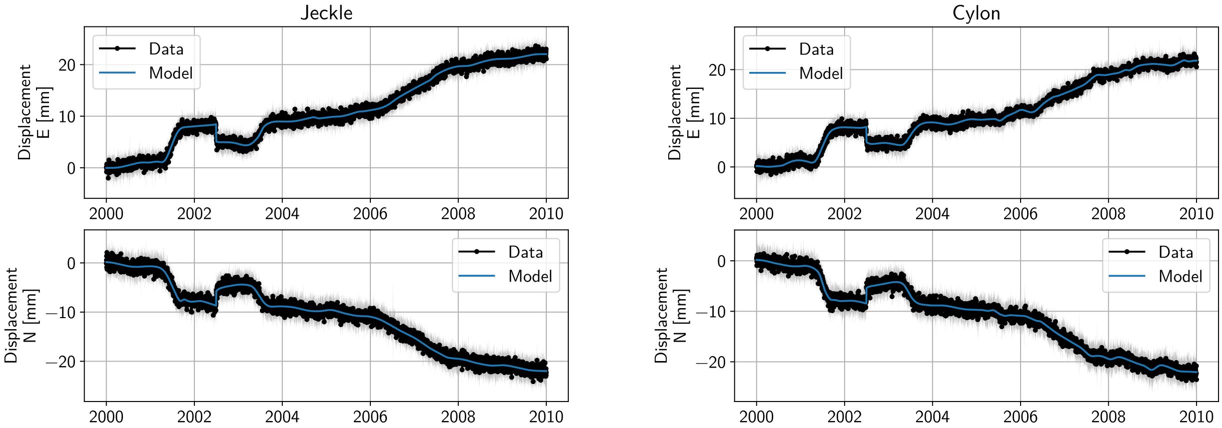

(c) Jeckle, Local L0 **(d)** Cylon, Local L0

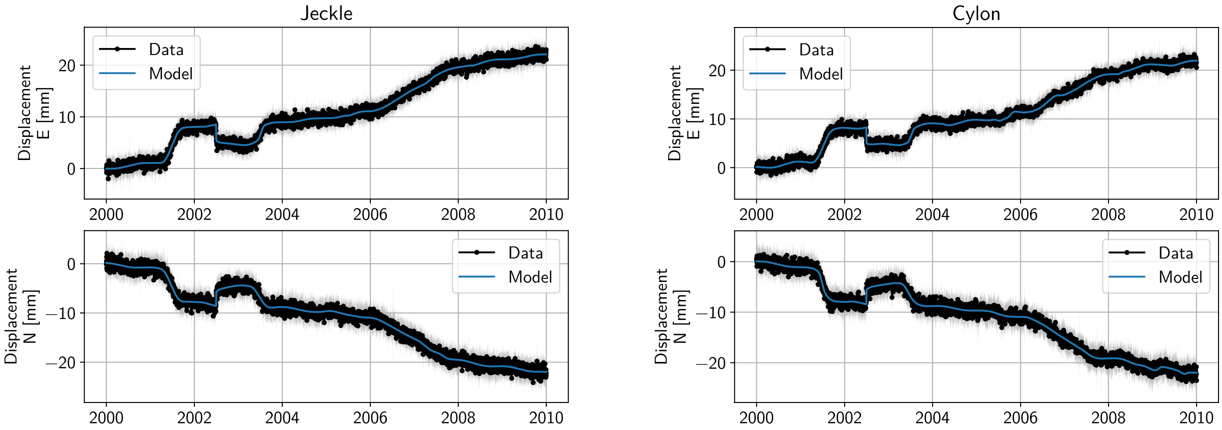

(e) Jeckle, Spatial L0 **(f)** Cylon, Spatial L0

Figure S3: Timeseries comparison for the two neighboring stations Jeckle and Cylon and three regularization schemes in the two east and north components. Black dots are the synthetic observations, with the grey shading corresponding to three standard deviations of simulated observation uncertainty. The blue line represents the final overall model fit. The fitted models are virtually indistinguishable between regularization schemes, except for the overfitting of some colored noise at station Cylon, which is reduced with the spatial L0 regularization.

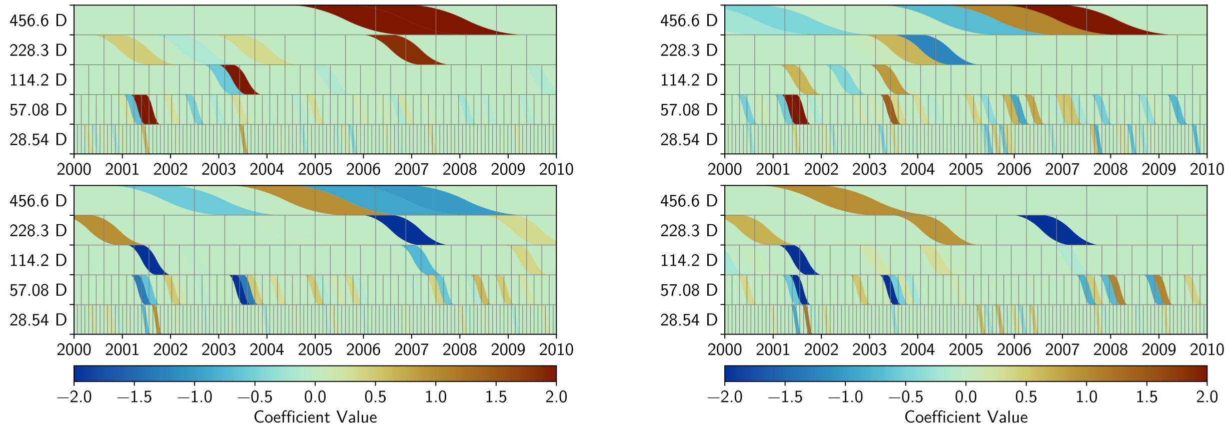

(a) Jeckle, L1

(b) Cylon, L1

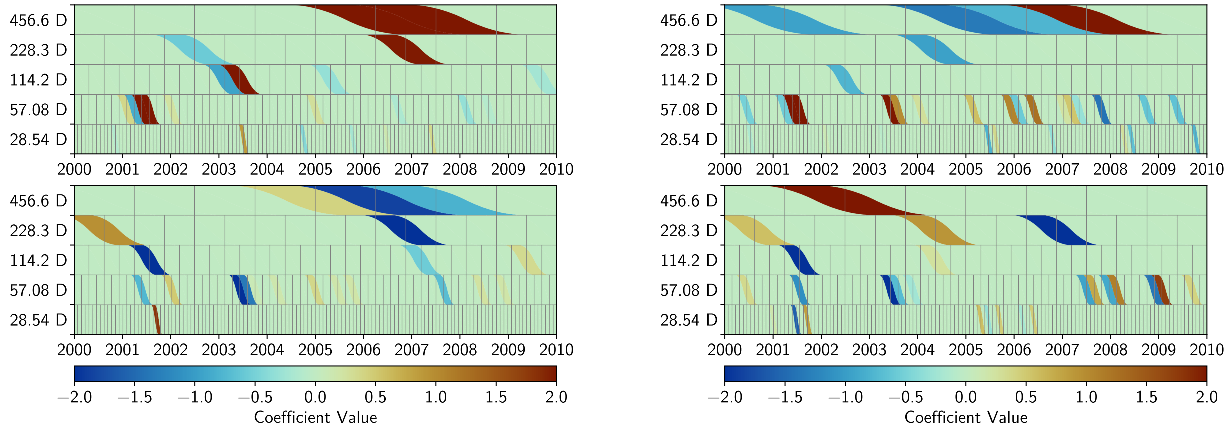

(c) Jeckle, Local L0

(d) Cylon, Local L0

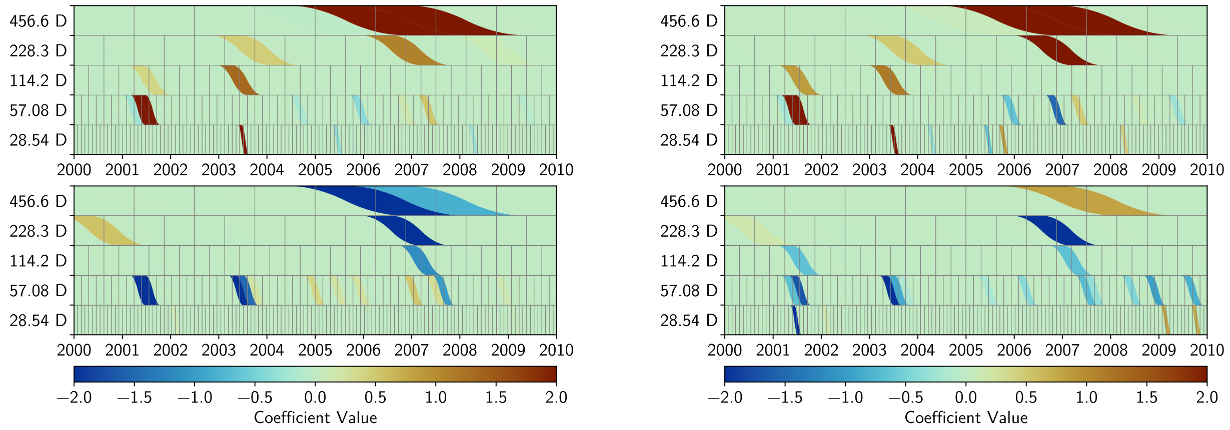

(e) Jeckle, Spatial L0

(f) Cylon, Spatial L0

Figure S4: Scalograms of the transient model for the stations and regularization in Fig. S3. The horizontal and vertical axes correspond to time and the discrete periods of the splines, respectively. Patches (colored by the spline coefficient's value) in this time-period-space represent a single spline in the dictionary, with their extent in time defined as the active period of the spline (i.e., having non-zero gradient), and their height defined by the relative magnitude of the particular spline compared to all splines active at that time. Using the L1 solver, the transients (two shortterm, one longterm) are sparsely fitted in time, but not in space (i.e., each station's timeseries is fit using different splines). The local L0 regularization does not change this general behavior. Spatial L0 regularization leads to the transients being sparsely fitted in time *and* space (i.e., every station's timeseries is fit with a similar set of splines). Modeling the transients with coefficients sparse in time, space and period is beneficial in the context of identifying signals close to the noise floor that are appearing at multiple stations, since the respective coefficients will be penalized less, allowing for a more physically-consistent decomposition. Conversely, the penalization of coefficients that are only seen at isolated stations makes it easier to identify local shortterm noise processes.

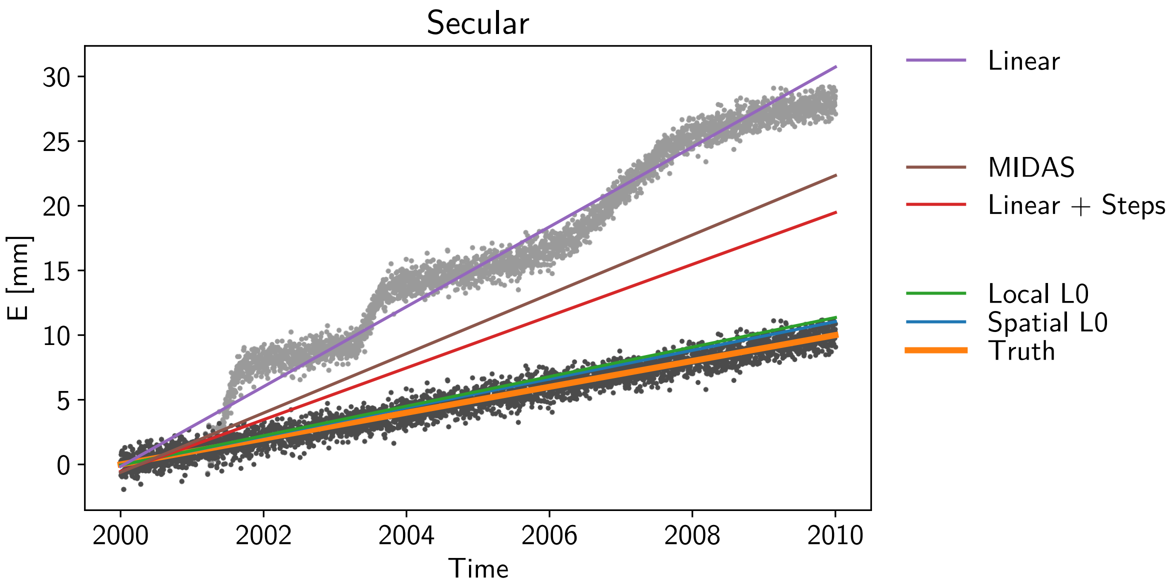

Figure S5: Comparison of the secular velocity estimates (East component) presented in Section 4.1, Fig. 2 with other methods. The dark gray dots correspond to the sum of true secular velocity and the generated noise; the light gray dots additionally include the transient constituents. The true secular velocity (orange line) and secular velocity estimated by the spatial L0 solver (blue line) correspond to the same lines in Fig. 2. The secular velocity estimated by the local L0 solver (compare Fig. 3) is shown with the green line (essentially overlapping the spatial L0 result). The three other lines correspond to other commonly used methods: local, unregularized least squares with (red) and without (purple) steps at the transient center times (assumed to be known); and the MIDAS solution (brown). In our synthetic example, the presence of the transient signal throughout most of the considered timeseries is significant enough to heavily deteriorate the estimated produced by the simple least squares as well as the MIDAS methods. For this station, and in the east component, adding spatial awareness only provides a minimal benefit, although Table S1 shows that across components and stations, there are significant benefits.

	East [mm/a]	North [mm/a]
Spatial L0	0.108107	0.227728
Local L0	0.456424	0.512325
Linear + Steps	0.623014	0.605845
Linear	1.275072	1.272709
MIDAS	0.854414	0.871200

Table S1: Root-Mean-Squared-Error between the secular velocity estimates and the true secular velocity, averaged across the entire network, for the methods presented in Fig. S5, and both data components individually. The spatial L0 solution significantly outerperforms the other solutions (including the local L0 solution).

S.2 Influence of Number of Stations

The code for this analysis, the synthetic model parameters, as well as the exploration of additional explored hyperparameters, can be found in Tutorial 5 of the online documentation.

In this section, we use a synthetic network of $N = 20$ stations, distributed randomly, that is only affected by a single transient process and white noise, to explore the dependence of the model error on the number of stations used. The noise level relative to the maximum amplitude of the transient signal, σ, is one of the hyperparameters we vary. The other variable is the number of stations $2 \leq n \leq N$ used by the spatial L0-regularized solver. For each test case, we therefore subsample the original network to create a subnetwork of smaller size n, comprised of randomly selected stations. (We also calculate the result of using a local L0-regularized solver for comparison, where by construction $n = 1$). The number of samples m, for each n to test, is given by the maximum of either the amount of possible permutations, or a defined maximum value M based on computational considerations ($M = 50$ in our case).

For each σ and each n, we therefore have m samples to test. The metric we choose to compare is the root-mean-squared true model error (RMSE), calculated from the final fit of each sampled subnetwork (ensuring the solvers iterate long enough to converge). For each n, we therefore compute the double mean of the RMSE, ϵ, first across the subnetwork, and then across samples. We also compute the standard deviation σ_ϵ of the samples of the subnetwork-wide mean RMSEs.

Fig. S6 shows the results of our experiment. For all of the cases, the mean RMSE ϵ decreases with increasing number of stations used in the fitting process (approximately by $1/\sqrt{n}$). Furthermore, the variance of the errors decreases as well. Importantly, for the case of $\sigma = 3$ (i.e., the white noise standard deviation is three times the maximum magnitude of the transient signal), the local L0-regularized solution has a high error variance centered close to the maximum allowable error (defined as not fitting a transient at all). Including multiple stations in the estimation process, however, decreases the mean error and error variance significantly — with 20 stations, as low as the mean error for the local L0-regularized solution for $\sigma = 1$. In the highest noise case presented here, $\sigma = 10$, most local L0-regularized solutions actually overfit the data. Incorporating spatial awareness prevents the solver to do so. Overall, as shown by the reduction of error, error variance, and susceptibility to overfitting, the importance of using spatial awareness for transient model fitting becomes clear.

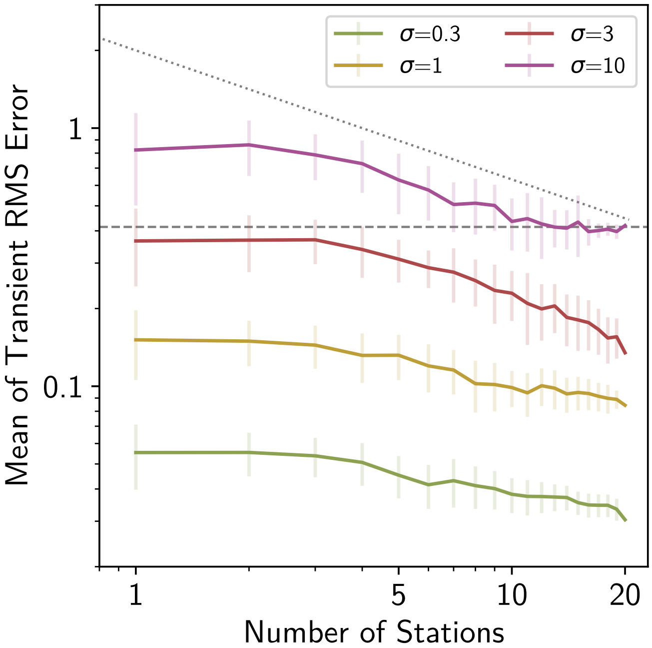

Figure S6: Sample mean (ϵ, colored lines) and sample standard deviation (σ_ϵ, vertical errorbars) for all the sampled subnetworks as a function of the number of stations used in the solution process (n, horizontal axis), and noise level ratio (σ, different colors). The dashed, horizontal grey line corresponds to the maximum allowable error if no transient signal is fitted at all. The dotted grey line is a reference line parallel to $1/\sqrt{n}$.

S.3 Long Valley Caldera: Secular Velocity Comparison

The code for this analysis can be found in Example 2 of the online documentation.

S.3.1 Method

Qualitatively, our results of transient and seasonal constituents are comparable to, e.g., Ji et al. (2013); Montgomery-Brown et al. (2015); Silverii et al. (2020). To quantitatively validate the decomposition of the input timeseries from the Long Valley Caldera Region (LVCR) into its different constituents, we would need published, already-decomposed timeseries for the same study area. However, we are not aware of such products, and reproducing decompositions based on individual studies is beyond the scope of the paper.

A different way to still be able to perform a quantitative validation of our method is to recognize the fact that if our method is successful at distinguishing motion due to transient processes from longterm, secular motion (while still taking into account seasonal, seismic, and maintenance signals), then such estimates of secular motion should be free of physical influences other than longterm plate motion and deformation. Specifically for the Long Valley Caldera, we would expect that on top of a "background" field of motion, we would not see any influence from the magmatic caldera inflation. (Of course, if the caldera intrusion has a steady-state component, we would have no way of inferring this from only GNSS data, and are therefore neglecting this possibility.)

Geodetically, we can fit an average field of motion by assuming our study area (a circle of 100 km radius around the caldera center) is, to first order, approximated by a rigid body moving on a sphere. We can then estimate a best-fit rotation matrix (or equivalently, an Euler pole) using standard weighted least-squares (e.g., Goudarzi et al., 2014).

In this section, we compare the results obtained using DISSTANS and its spatiotemporal L0 regularization approach with published MIDAS-derived secular velocities (Blewitt et al., 2016) and the Geodesy Advancing Geosciences and EarthScope (GAGE) facility's secular velocities (Herring et al., 2016). We first build a **`Network`** object that contains all three different velocity models. Then, the `Network.euler_rot_field()` method calculates the predicted velocity due to best-fit motion on a spherical Earth. Lastly, we remove the best-fit "background" secular velocities from the previously estimated, "model" secular velocities to produce "residual" secular velocities. The smaller these residuals, the better can our study area be approximated by a rigid plate.

In our comparison, we do not include methods that rely on a priori removal of a secular velocity in order to extract the transient. These approaches currently represent the majority of transient extraction methods; e.g., in combination with filtering (e.g., Silverii et al., 2020), with vbICA (e.g., if the timeseries is strongly correlated, Gualandi et al., 2016), with Singular Spectrum Analysis (SSA, e.g., Walwer et al., 2016), or with stacking (e.g., Kano and Kato, 2020). We omit these methods on the basis that they either do not claim to capture the longterm secular velocity in the first place (e.g., because the analyzed timespans are short, Kano and Kato, 2020) or that they are heavily reliant on assumptions (e.g., assuming a certain timespan represents steady-state velocity, Silverii et al., 2020).

S.3.2 Results

We first want to note that neither the MIDAS nor the GAGE solution explicitly aim to model transient processes, with the exception of postseismic, decaying transient motion. While MIDAS does aim to be robust against shortterm transients, in general, our comparison is therefore not a "fair" one — both MIDAS and GAGE velocity fields are estimated in a fully-automated fashion and for the majority of global GNSS stations, they provide high-quality, reliable secular velocity estimates. The goal of this subsection is simply to highlight the differences in model results owing to our explicit modeling of transient processes.

	DISSTANS	MIDAS	GAGE
All	2.692	3.065	3.883
Outside LVCR	2.880	2.788	2.789
Inside LVCR	2.490	3.318	4.730

Table S2: Root-Mean-Squared (RMS) residual magnitudes (in mm/a) between the modeled and background horizontal secular velocities for this study (DISSTANS) as well as the published velocities from MIDAS (Blewitt et al., 2016) and GAGE (Herring et al., 2016). The rows correspond to different subsets of the data over which the RMS is calculated. "Inside LVCR" corresponds to the stations shown in the lower panels of Figs. S7–S9, "All" to the ones shown in the upper panels of Figs. S7–S9, and "Outside LVCR" to the ones that are in the latter but not in the former. For stations outside the LVCR, the models produce approximately the same residual RMS (approx. ± 3%), but within the LVCR, DISSTANS reduces the residuals by approx. 25–47%, respectively.

Fig. S7 shows the modeled horizontal secular velocities from the DISSTANS, MIDAS, and GAGE solutions. While over the entire study region, the velocities mostly match each other, differences are obvious when zooming into the Long Valley

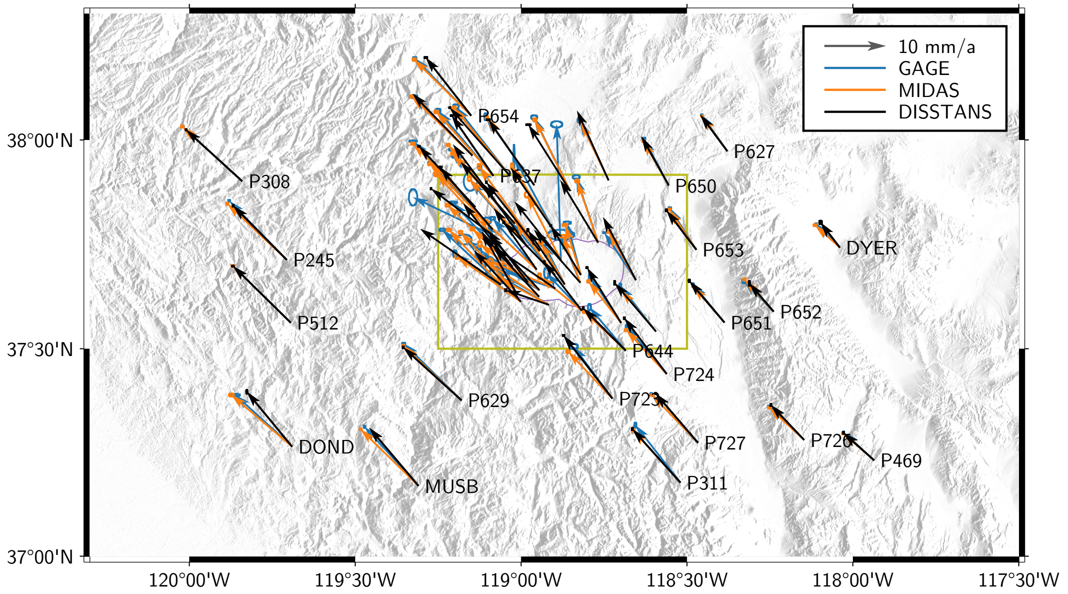

(a) Model (Study Region)

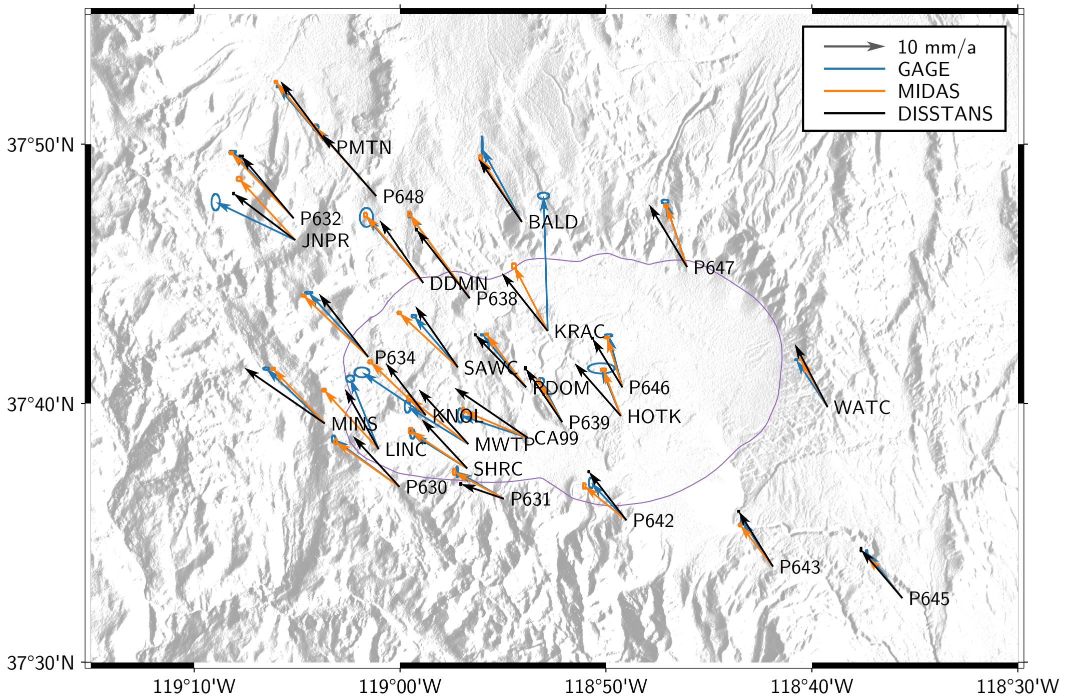

(b) Model (Long Valley Caldera Region)

Figure S7: Upper panel: Modeled horizontal secular velocities in the study region for the three different solutions DISSTANS (Section 4.2), MIDAS (Blewitt et al., 2016), and GAGE (Herring et al., 2016) (in GAGE's North America-fixed reference frame). The Caldera ring fault (USGS Quaternary Fault Database, Bailey, 1989) is shown in purple. Uncertainties are shown as one-standard-deviation ellipses for each solution. The green rectangle shows the extent greater Long Valley Caldera Region (LVCR). Lower panel: Same as upper, zoomed into the LVCR. While the DISSTANS-derived velocities mostly match the published velocities outside the LVCR, they are significantly different within the LVCR.

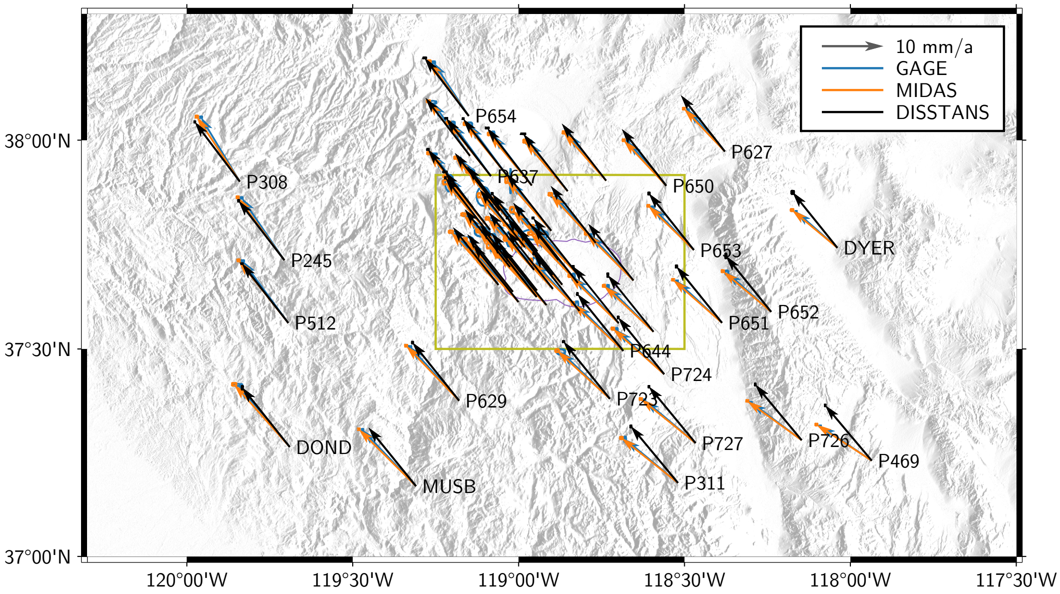

(a) Background (Study Region)

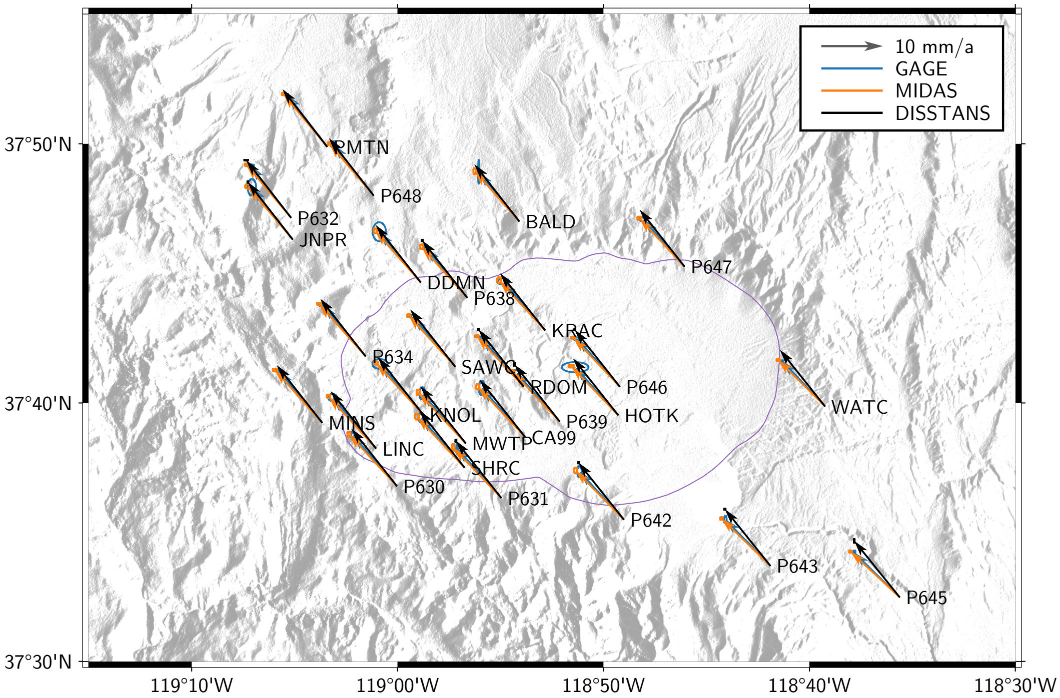

(b) Background (Long Valley Caldera Region)

Figure S8: Background velocity fields as calculated by the best-fit Euler pole for the entire study area and the Long Valley Caldera Region in the upper and lower panels, respectively. Uncertainties, fault oulines, and colors are the same as in Fig. S7. The DISSTANS-derived background velocity field slightly differs from the MIDAS- and GAGE-derived fields, but exhibit the same overall pattern.

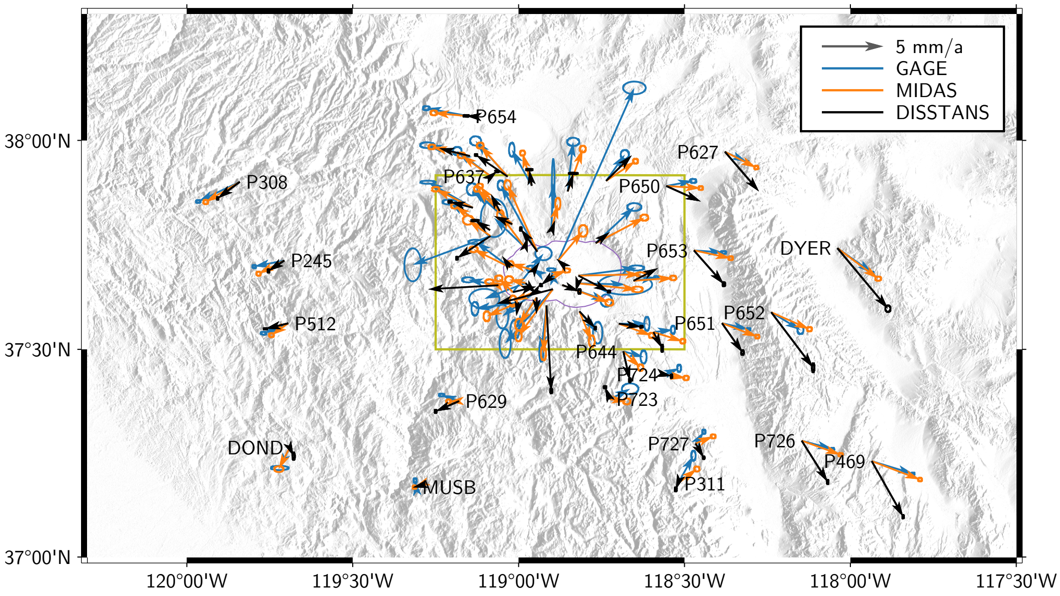

(a) Residuals (Study Region)

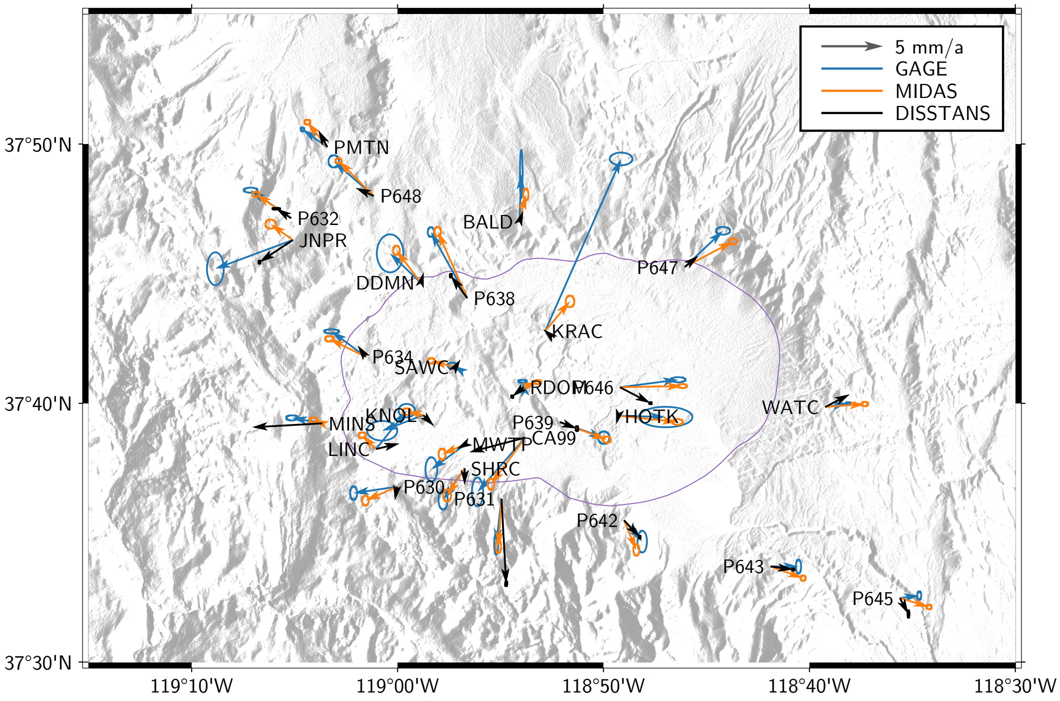

(b) Residuals (Long Valley Caldera Region)

Figure S9: Residual secular velocities for the entire study area and the Long Valley Caldera Region (LVCR) in the upper and lower panels, respectively. Uncertainties, fault oulines, and colors are the same as in Fig. S7. The DISSTANS solution has smaller residual velocities in the LVCR than the MIDAS and GAGE solutions. (Note the different vector scale length.)

Caldera Region (LVCR) itself. Calculating the best-fit velocities assuming a rigid-body motion for the three different solutions (independently) yields similar results (Fig. S8) (differences around or below millimeter/year level). Excluding stations inside the LVCR in the estimation process also does not affect the resulting velocities significantly (differences on the order of half a millimeter/year).

Fig. S9 shows the residual velocities (difference between modeled horizontal and best-fit background velocities). Qualitatively, the residuals from the DISSTANS solution are visibly reduced inside the LVCR compared to the MIDAS and GAGE solutions. Specifically, the MIDAS and GAGE solutions show a clear expansion component for stations in or near the caldera itself; this expansion pattern is much less prominent in the DISSTANS solution. Outside of the LVCR, all residuals show coherent patterns of motion, indicative of the imperfection of the assumption on the background velocity field (see below). Table S2 quantifies the differences between model residuals using the Root-Mean-Square (RMS) of the residual magnitudes (i.e., the length of the residual vectors). Crucially, in the LVCR, where we expected the residuals to decrease by modeling the transients explicitly, we find that they are reduced by 25–47% (depending on the model). This reduction implies that the original modeled secular velocity field produced by DISSTANS more closely approximates the homogenous background velocity field. The reduction of residuals inside the LVCR is accompanied by only a small increase in residuals of about 3% outside the LVCR. Interestingly, the residual RMS of our velocity model is more similar between stations outside and inside the LVCR (range of 0.4 mm/a), whereas the residuals of the MIDAS and GAGE solution show a larger variance (ranges of 0.5 and 1.9 mm/a).

Overall, we interpret the reduction of residuals in the Long Valley Caldera Region for the DISSTANS solution to demonstrate the benefit of spatial awareness and explicit modeling of transient processes. By separating transient from longterm motion in a spatially-aware framework, the resulting secular velocity field is more homogenous than the MIDAS and GAGE solutions, and diminishes significantly the effect of magmatic inflation periods on the secular velocity estimate in the vicinity of the caldera.

S.3.3 Note on the assumed background velocity field

By comparing the secular velocities instead of the displacement timeseries during transient episodes, we are able to show quantitative differences between our solution and two other published secular velocity fields — the MIDAS (Blewitt et al., 2016) and GAGE (Herring et al., 2016) models. To demonstrate the effect of explicitly modeling transient processes on the resulting estimed secular station velocities, we have furthermore estimated and removed a “background” field of motion from the secular velocities, and shown the residual velocities. We take the background field of motion to be the best-fit velocity field for our small study area (100 km radius around the Long Valley Caldera center), assuming rigid body motion on a sphere. Note that we do not assume the background velocity field to represent the true underlying longterm velocity (e.g., we expect distributed shearing in our study area because of the remote North America-Pacific plate boundary), only that such a velocity field should be able to reproduce the modeled secular velocities to first order (which is the case). The estimation of the background velocities is performed using simple, unregularized, weighted least-squares. The results obtained from the three different input fields (DISSTANS, MIDAS, and GAGE) are similar, supporting our assumption that the background field is able to capture most of the secular velocity signal. Therefore, using the residual velocity fields for our comparison simplifies the highlighting of the differences between the processing strategies of the three secular velocity models.

S.4 Long Valley Caldera: Seasonal Signals

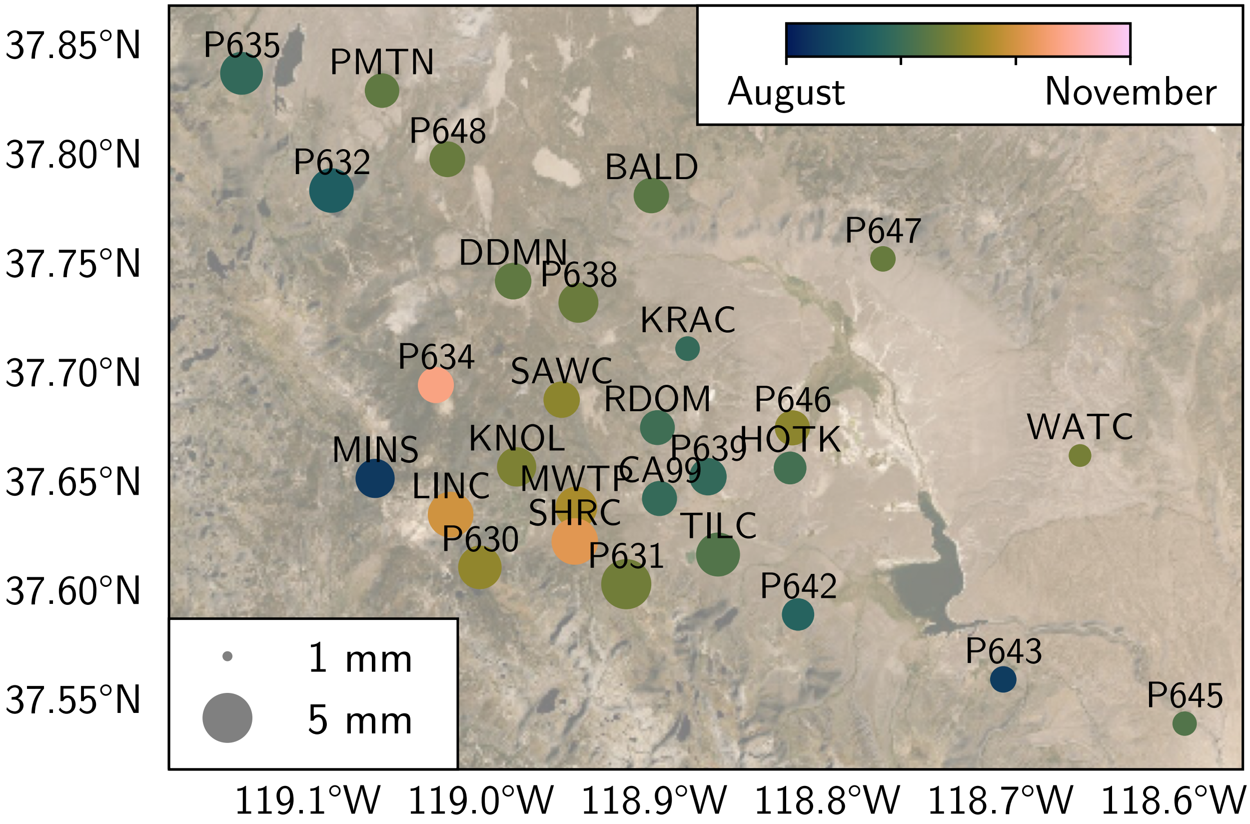

Figure S10: Unregularized (average) component of the vertical seasonal fitted annual model. The marker size corresponds to the amplitude, and the color corresponds to the time of the sinusoid's maximum during the year. Background satellite imagery by Earthstar Geographics & Esri.

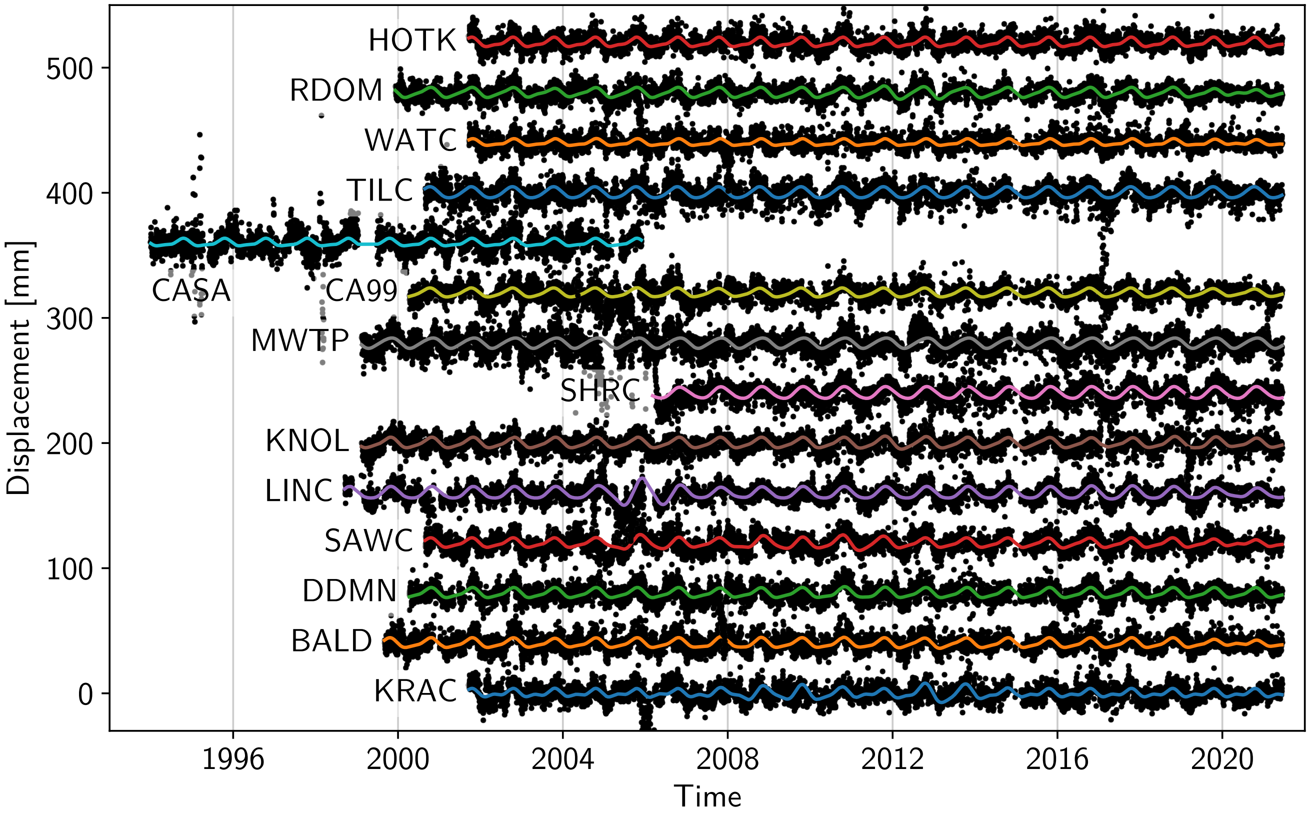

Figure S11: Full vertical seasonal model (unregularized and regularized, annual and semi-annual) for the selected stations from Fig. 5, in the same order. Black dots are the overall model's residuals, centered on the seasonal model.

References

Bailey, R.A., 1989. Geologic map of the Long Valley caldera, Mono-Inyo Craters volcanic chain, and vicinity, eastern California. IMAP doi:10.3133/i1933.

Blewitt, G., Kreemer, C., Hammond, W.C., Gazeaux, J., 2016. MIDAS robust trend estimator for accurate GPS station velocities without step detection. Journal of Geophysical Research: Solid Earth 121, 2054–2068. doi:10.1002/2015JB012552.

Goudarzi, M.A., Cocard, M., Santerre, R., 2014. EPC: Matlab software to estimate Euler pole parameters. GPS Solutions 18, 153–162. doi:10.1007/s10291-013-0354-4.

Gualandi, A., Serpelloni, E., Belardinelli, M.E., 2016. Blind source separation problem in GPS time series. Journal of Geodesy 90, 323–341. doi:10.1007/s00190-015-0875-4.

Herring, T.A., Melbourne, T.I., Murray, M.H., Floyd, M.A., Szeliga, W.M., King, R.W., Phillips, D.A., Puskas, C.M., Santillan, M., Wang, L., 2016. Plate Boundary Observatory and related networks: GPS data analysis methods and geodetic products. Reviews of Geophysics 54, 759–808. doi:10.1002/2016RG000529.

Ji, K.H., Herring, T.A., Llenos, A.L., 2013. Near real-time monitoring of volcanic surface deformation from GPS measurements at Long Valley Caldera, California. Geophysical Research Letters 40, 1054–1058. doi:10.1002/grl.50258.

Kano, M., Kato, A., 2020. Detailed Spatial Slip Distribution for Short-Term Slow Slip Events Along the Nankai Subduction Zone, Southwest Japan. Journal of Geophysical Research: Solid Earth 125, e2020JB019613. doi:10.1029/2020JB019613.

Montgomery-Brown, E.K., Wicks, C.W., Cervelli, P.F., Langbein, J.O., Svarc, J.L., Shelly, D.R., Hill, D.P., Lisowski, M., 2015. Renewed inflation of Long Valley Caldera, California (2011 to 2014). Geophysical Research Letters 42, 5250–5257. doi:10.1002/2015GL064338.

Silverii, F., Montgomery-Brown, E.K., Borsa, A.A., Barbour, A.J., 2020. Hydrologically Induced Deformation in Long Valley Caldera and Adjacent Sierra Nevada. Journal of Geophysical Research: Solid Earth 125, e2020JB019495. doi:10.1029/2020JB019495.

Walwer, D., Calais, E., Ghil, M., 2016. Data-adaptive detection of transient deformation in geodetic networks. Journal of Geophysical Research: Solid Earth 121, 2129–2152. doi:10.1002/2015JB012424.